Investigations of a timing silicon particle detector

Bachelor Thesis

in the Institute of nuclear physics
at the Universität Münster

submitted by
Robert Jesse Kossmann

Universität Münster
AG ANDRONIC

January 2024

First referee: Prof. Anton Andronic
Second referee: Apl. Prof. Christian Klein-Bösing

Contents

1. Introduction

As Captain Kathryn Janeway in the series Star Trek: Voyager quite suitably puts it, "The purpose of all this [technology] is to help us gain knowledge about the universe". This is also true for the Low Gain Avalanche Detector, in short LGAD, which is supposed to be used in particle physics, where high temporal and spatial precision with a low noise level is needed to understand the rudimentary mechanics of the universe. The LGAD fulfils these criteria and as such is, although being a rather new technology, already planned for upgrades of existing and for new experiments.
LGADs are already in use in the HADES (High Acceptance Di-Electron Spektrometer) at GSI (Gesellschaft für Schwerionenforschung) in Germany for temporal resolution. They are also planned for upgrades of the CMS (Compact Muon Solenoid) and ATLAS (A Toroidal LHC ApparatuS) experiments at CERN (European Organization for Nuclear Research), which are detectors for high energy particle collisions [Sun+20][18].
HADES itself is a detector for the events generated in a collision on a gold foil target by ions accelerated by the linear accelerator UNILAC (UNIversal Linear ACcelerator) and the ring accelerator SIS (Schwerionensynchrotron). In tests outside the experiment, accuracies better than 100 ps were achieved. When introduced in the experiments, a resolution of 115 ps was calculated, which, while worse than previously achieved outside, was still very precise. The degration of precision was allocated to the environmental noise due to the high beam intensity in the collisions [Krü+22].
Additionally, it is also being tested if the LGAD can be used in ion beam therapy, which requires spatial resolution while having high detection and measurement rates. Ion beam therapy exploits the penetration depth of ions in matter by aiming the Bragg peak, where the majority of ions are absorbed, at tumours, while leaving the travelled through matter mostly intact in comparison to the use of photons. To track particle trajectories through a patient and separate residual energy loss, LGADs could potentially be used in iCT (ion Computed Tomography), a method similar to X-ray CTs (X-ray Computed Tomography) intended for imaging the inside of a patient's body. The proposed idea of iCT is to use the same ions as the ion beam therapy, allowing for more precision and a better understanding of the interaction between the ions and the target area. An iCT consists of a tracking system for the particle trajectory and a detector to measure energy-loss with a spatial resolution [Krü+22].
Overall, while LGADs are new in comparison to established gas and other semiconductor detectors, their use in the areas of temporal and spatial resolution as well as their radiation hardness and the low noise show great promise in a varied field of applications from particle physics to medicine.

To test the LGAD, measurements with cosmics and an $^{55}_{26}$Fe source will be made, allowing investigations into the main functions capabilities by measurements of the noise and the rise time. Also, measurements for the energy resolution are being made, but while no high precision is expected, the measured signal should show an amplitude dependent on the deposited energy. If successful, this allows better and more specified use of the LGAD. If not successful, problems can be found and identified for further investigation for upgrades.

2. Theoretical Background

In this chapter the theoretical background, necessary for comprehension of the experiments and the following results, is laid out. To understand the detection of radiation with the Low Gain Avalanche Diode (LGAD) specifically, understanding the interaction between radiation and matter as well as the basics of silicon detectors are needed. Unless stated otherwise, the following chapters are based on [Her16].

2.1. Interaction of Particles with Matter

When charged particles pass matter, energy is lost due to ionization, bremsstrahlung and excitation of atoms. The description of the energy loss over a path x, also known as stopping power, is described by the Bethe-Bloch-Formula:

$$-\left\langle \frac{dE}{dx} \right\rangle = K\frac{Z}{A}\rho\frac{z^2}{\beta^2}\left(\frac{1}{2}\ln\frac{2m_e c^2\beta^2\gamma^2 T_{Max}}{I^2} - \beta^2 - \frac{\delta(\beta\gamma)}{2} - \frac{C(\beta\gamma, I)}{Z}\right) \quad (1)$$

The variables describing the energy loss are the constant factor K = 0.307 $\frac{MeV\ cm^2}{mol}$, the velocity $\beta = \frac{c}{v}$, the electric charge z of the particle, the mean ionization energy, the atomic charge and the mass number of the matter I, Z and A, the maximal transferred energy in a central thrust T_{max}, the density correction for high energies δ and lastly the shell correction C/Z, which is important for low particle speeds.
In practice, it is to be said that the energy deposited by a particle in a silicon detector is not equivalent to the total energy measured by the detector as the amplitude. This is due to the detector only being able to measure the charge created by the ionization of the particle, as excitation and breaking radiation will also result in an energy loss which is not represented in the signal send.
Also important, are effects of thin or thick silicon detector layers. In thick layers the probability of collisions with a high energy transfer is higher, so the probability of electrons, freed by collisions, being able to create further ionization due to collisions with enough energy, also known as δ-electrons, is high, resulting for the deposited energy not in a gaussian distribution but a Landau distribution. If the layer is thin, the probability for this process is lower. It is also possible that a particle does not deposit all of its energy into the silicon and leaves the detector with sufficient energy. [Sch19]

2.2. Interaction of Photons with Matter

When photons pass matter, different effects are possible, changing the energy of the photons or absorbing it completely. The occurring effects are the Photoeffect, the

Coulomb effect and the pair production, depending on the energy of the photon. The approximate shares of absorption are seen in fig. 1 for lead and carbon. The effect of Rayleigh scattering is also present, but the energy transferred in this process is so small that it is not of relevance for particle detection and as such is ignored [Sch19].

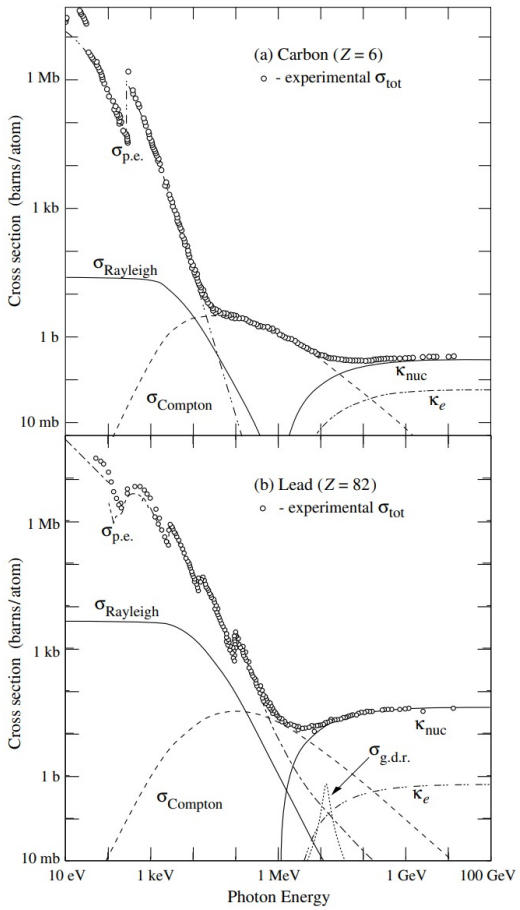

Figure 1: Representations of the experimentally deduced cross-sections and their specific effects, with $\sigma_{p.e.}$ describing the photoeffect with the shells and $\sigma_{g.d.r.}$ for the photoeffect with the nucleus, $\sigma_{Rayleigh}$ describing the effect of Rayleigh scattering, $\sigma_{compton}$ the Combton effect, and lastly pair production with the shell by K_e and with the nucleus by K_{nuc}. Taken from source[Her16].

2.2.1. Photoelectric effect

The photoelectric effect describes the complete transfer of the energy of the photon to an electron in a bound state in an atom. The free electron as such has to overcome the binding energy in its state E_B. When the electron is no longer bound, the energy surplus is transferred into kinetic energy. This energy can be easily calculated following the following formula:

$$T_e = E_\gamma - E_B \tag{2}$$

As the kinetic energy cannot be negative, the transmitted energy of the photon must be greater than the binding energy of the electron in the atom. When looking at the cross-section depending on E_γ, for the Photoeffect this results in a sharp rise of the cross-section, each time a new energy level is reached. This means a bound state, with a different binding energy E_B, can be reached, allowing interaction with more bound electrons in the passed matter. This is seen well in the cross-section diagrams for Carbon and Lead provided in fig. 1. Due to the high mass of the nucleus in comparison to the electron, the recoil of the electron emission to the core can be neglected with little inaccuracy. The cross-section is vastly dependent on the nuclear charge Z and on the energy of the photon with $\sigma \sim Z^5 E_\gamma^{-3.5}$ for $E_\gamma \ll m_e$ or $\sigma \sim Z^5 E_\gamma^{-1}$ for $E_\gamma \gg m_e$ [Sch19].

2.2.2. Compton scattering

Compton scattering describes scattering of photons on free electrons or effectively free electrons in relation to the energy of the photon. The energy of the photon after the scattering event is given by the following formula with the photonenergy E_γ and the particle constant $\epsilon = E_\gamma / m_e c^2$:

$$E_\gamma^* = \frac{E_\gamma}{1 + \epsilon(1 - cos(\theta_\gamma))} \tag{3}$$

The cross-section is described by the Klein-Fishing-Formula with the additional constant of the classical electronic radius r_e:

$$\frac{d\omega_C}{d\Omega_\gamma} = \frac{r_e^2}{2[1 + \epsilon(1 - cos\theta_\gamma)]^2} \left(1 + cos^2\theta_\gamma + \frac{\epsilon^2(1 - cos(\theta))^2}{1 + \epsilon(1 - cos(\theta_\gamma))} \right) \tag{4}$$

The cross-section of Compton scattering has a linear correlation with the atomic number $\sigma \sim Z$ of the absorbing material and an inverse correlation of $\sigma \sim 1/E_\gamma$ with the photon energy. This can be seen well in fig. 1.

2.2.3. Pair production

Pair production describes the process of the photon using its energy to split into an electron and a positron. Due to conservation of momentum, a second object receiving the recoil of the emission is needed for pair-production, this is in most cases the nucleus of an atom. The energy needed to create pair production is the energy of two electrons plus the recoil energy. However, as the recoil energy can be mostly neglected when it is transmitted to an atomic nucleus resulting in a lower energy limit of:

$$E_{min} \approx 2m_e c^2 = 1.02\,\mathrm{MeV} \tag{5}$$

As the used photon source $^{55}_{26}\mathrm{Fe}$ (cf. section 4.5) has a photon energy far lower than this, pair production cannot appear in the course of this thesis.

2.3. Silicon Detectors

Silicon particle detectors are used as semiconductor detectors. The investigated silicon particle detector is an LGAD silicon strip detector chip, which will be explained in detail later. Semiconductor detectors are used in high precision experiments like in the HADES experiment at the GSI. Advantages of Semiconductor detectors include high spatial and temporal resolution, high signal to noise ratios and, in the case of silicon detectors, high radiation resistivity. The high signal to noise ratio is achieved by creating a pn-junction with a depletion zone so that no signal other than the electron-hole-pairs created by passing particles can be detected. All this will be explained below.

2.3.1. Semiconductors

A material is able to conduct current if energy levels in the conduction band are filled with charge carriers. The conduction band and the valence band are a description for bound and not bound energy levels for electrons in matter. This is shown well in fig. 2. Electrons in the conduction band therefore are not bound and as such can flow as a current. Insulators show a great energy gap between the valence band and the conduction band, while in conductors the energy gap is very narrow or the bands are even overlapping, as in the example. Semiconductors themselves are not assignable to either type as they feature an energy gap of about 1 eV varying with the materials used.

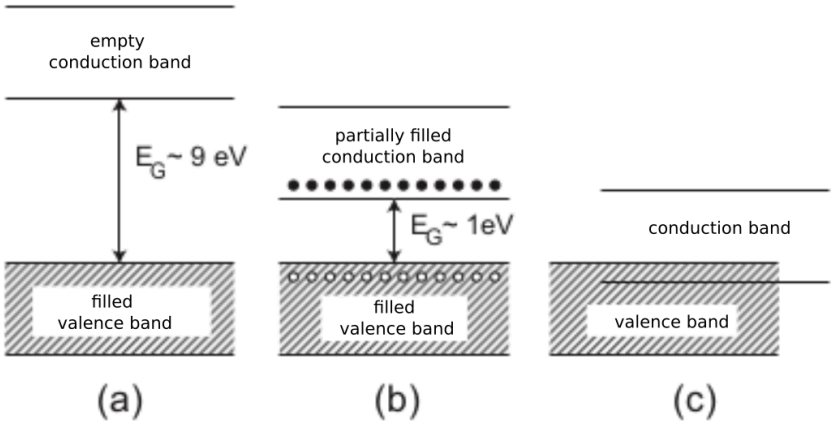

Figure 2: Schematic representation of the energy levels in an insulator (a), semiconductor (b) and conductor (c). The figure is taken and translated from source [Her16].

Since the energy of electrons is described with the fermi distribution, a varying fraction of electrons in semiconductors is always in the conduction band. As this amount in standard circumstances, meaning at about 293.15 K, is minuscule, semiconductors are not good conductors. With rising temperatures, the conductivity rises as statistically more charge carriers occupy energy levels in the valence band, resulting in general in a better conductivity of semiconductors at higher temperatures.

2.3.2. pn-junction

A pn-junction is created by doping a semiconductor, typically silicon, which will henceforth be used for explanation, with atoms from the 5th or 3rd main-group. This is done due to the additional or missing valence electron in comparison with the 4 valence electrons of silicon, creating artificial energy levels with different energy gaps. Doping in this context means the substitution of a semiconductor atom in the semiconductor crystal. Two types can be achieved here, p-doping with a missing electron in the crystal, or better described as a hole and n-doping with an additional electron in the crystal structure. Most commonly, phosphor, creating n-doping, and boron, creating p-doping, are used to dope silicon wafers. The additional charge carriers and energy levels makes the flow of current at normal temperature possible, as holes and not bound electrons are available at 293.15 K. The pn-junction itself is the transition between an n- and a p-doted semiconductor. Important here is the fermi level, describing the highest occupied level in a material. The doping shifts the fermi level of the conduction- and the valence-band, as higher levels are created in n-doped regions filled with the surplus electrons

and lower levels are created in p-doped regions by the holes which are filled up. This results schematically in case a) as can be seen in fig. 3, as the fermi level of two adjacent sections is constant, due to the electrons filling the energetically lowest levels. The holes and the electrons of the doping create a difference in the charge distribution, resulting in recombination of the charge carriers in the middle and a zone known as the depletion region. When a particle now hits electrons with sufficient energy, the energy deposited in the electrons lift them to a not bound state, creating an electron-hole-pair. With external voltage, the created charge carriers are pulled to the connections outside the depletion region, creating a detectable difference in voltage. This is interpreted as a signal and as such can then be deduced as an event of particle interaction, making detection possible. So, for particle detection, case c) as shown in fig. 3 is used with an external voltage in blocking direction. This event results in measurable voltage changes, allowing particle detection with a dependence of deposited energy to the deposited energy of the diode. Also, as described before the depletion region does not have filled conduction bands, as electrons and holes recombine, except the charge carriers created by an event, resulting in low currents aside from the signal.

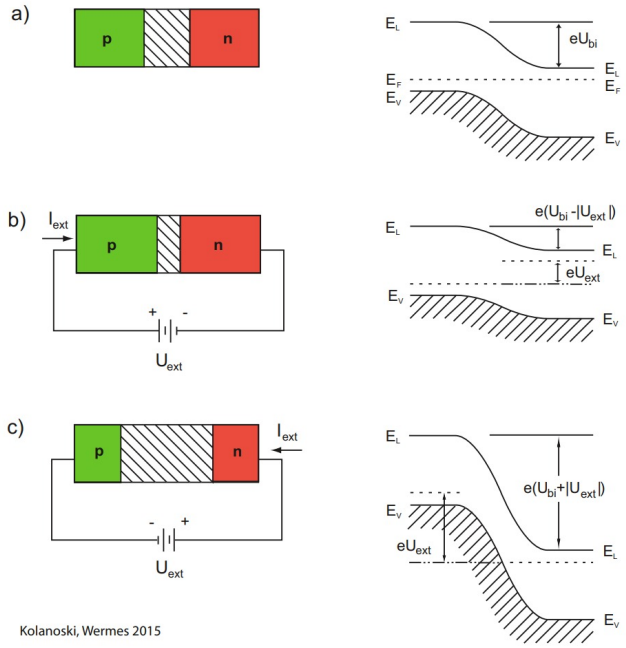

Figure 3: Schematic description of a pn-junction and resulting energy levels and their energy-gap $E = eU_{bi}$ with a) no external voltage, b) external Voltage U_{ext} in direction of the energy gap and c) external voltage U_{ext} in opposite of the energy gap. The figure is taken from source [Her16].

2.3.3. Silicon strip detectors

Silicon detectors all use the same method of electron-hole-pair generation, but they are distinguishable in the way the position of the interacting particle is detected. The used LGAD is a silicon strip detector, generally getting its name by the electrodes, which are placed as strips on top of silicon plates, known as wafer, as shown in fig. 4. When an interacting particle passes the depletion zone between the highly p-doted (p^+) and the highly n-doted (n^+) parts, electron-hole-pairs are created and drift individually to the aluminium electrodes on top and at the bottom of the wafer. The change in the voltage created can now be measured and interpreted as signals giving a one dimensional position, depending on the electrode receiving a signal. If multiple strips positioned next to each other receive signal at the same time, the position of the particle can be calculated even better by extrapolating it from the comparison of the shares of the two strips. This process is known as charge sharing.

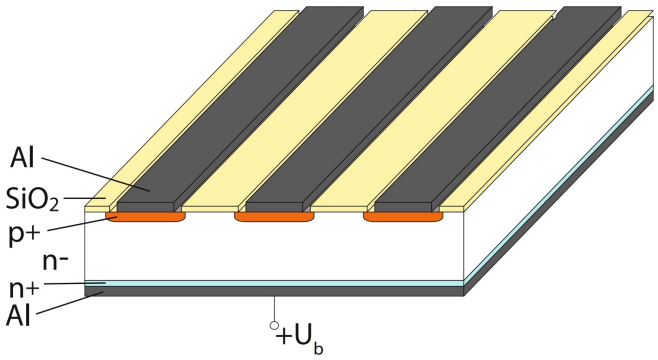

Figure 4: Schematic representation of a silicon strip detector. With aluminium (Al) electrodes and silicon dioxide (SiO_2) insulators. The figure is taken from source [Her16].

2.3.4. Avalanche Photodetectors

The Avalanche Photo Detector (APD) was created for low energy radiation detection. It introduces an internal amplification depending on the original signal amplitude. The gain factor in common APDs is between 10 to 100. However, with the amplification of the signal, the signal to noise ratio is much too small to be competitive to other modern detectors. [Mof+18]

2.3.5. Low Gain Avalanche Detectors

To lower the signal to noise ratio, a lower signal gain with a factor of 5-10 is needed and realised in the so called LGAD. To employ such a low amplification, the design of an LGAD differs from a standard silicon detector design, as shown in fig. 5. The electrodes are connected to heavily doted areas, with the cathode being n^+ and the anode being p^+. In the example shown, the electrodes for the LGAD would be connected to the top and the bottom of the schematic. The bulk and as such the detection area is weakly p doted to get a resistivity of $\sim$10 kΩcm preventing signal transmission which does not originate in a detection event. Between the bulk and the cathode, another p doted layer is present, with the doting concentrations shown in fig. 36. This results in a strong internal electric field where the signal gain takes place, while keeping the noise level low. The n^+ extensions, or rather gaps in the p-spray, are known as Junction Terminating Extensions (JTEs) and serve to control field effects at the edges of the cathode, creating a higher breakdown voltage. It is to be said that the p-spray in the example outside of the JTEs of each pixel can be interchanged with a heavily doted p^+ layer known as a p-stop. In both cases this is done to limit the extension of the dead region and stopping electron accumulation of neighbouring pixels [Mof+18], [Gia23].

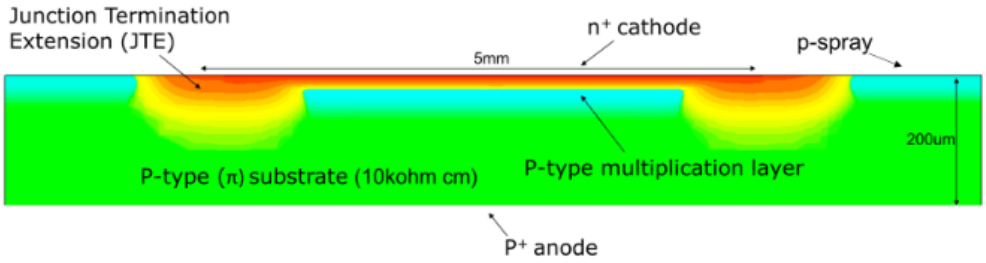

Figure 5: Schematic cross-section of LGAD strips. The figure is taken from source [Mof+18].

Variants of the LGAD While the LGAD boasts very precise timing resolution, problems like the JTE areas not being able to detect particles and as such not having a perfect fill factor for spatial resolution, result in further developments combating the problems. All these are taken from source [Gia23] and schematics, if possible, are shown in fig. 37.
The first example of this is the trench-isolated LGAD (TI-LGADs), fabricated by Fondazione Bruno Kessler (FBK, Trento, Italy). While details of the geometry have not been made public yet, trenches separating the pixels with an oxide filling are employed, achieving a fill factor of 75%.

Another alternative is the inverted LGAD (i-LGAD). Here, a good spatial resolution is achieved by creating a large n^+ layer which is only stopped at the edge of the sensor with a JTE. The hole collecting anodes, however, are used for signal detection and spatial resolution. This results in a fully active area and as such in a 100% fill factor. But for this method, the wafer needs to be processed on each side and needs to be thicker than the standard LGADs, resulting in a worse timing resolution, which was the originally intended use.
The capacity coupled LGAD (AC-LGAD) intents to address the dead region between pixels. This is done by also having a large n^+ layer as in the i-LGAD, but while the anode stays the same as in the standard LGAD, the cathodes are isolated with an oxide layer to the n^+ layer. Therefore, the electrons drift to a DC contact at the edge of the detector. The spatial resolution results of a capacity induced signal to electrode contacts through the oxide layer. Thereby, JTEs are only needed at the border of the detector and a fill factor of 100% is achieved. However, the AC-LGAD works most efficient in low-rate event environments.
The last presented LGAD is the deep-junction LGAD (Dj-LGAD). The Dj-LGAD is supposed to have a higher spatial resolution similar to the AC-LGAD but is intended for high rate event environments. The gain region here is not in the singular p-type layer but in a neighbouring p- and n-doted area, creating a narrow electric field with high amplification in the p-doted bulk. As such, the electric fields in the rest of the detector are rather low and no JTEs are required. A p-stop for pixel separation is still is nevertheless still in place. Due to the narrow amplification area, MIPs do not have enough gain to be detected. This variant has, however, not been finished and is currently under development.

3. The LGAD

In this section, the investigated LGAD is shortly characterized to give a better understanding for the later results. The basic functionality, as a standard LGAD, is already explained in section 2.3.5. The chip itself is seen in the middle of fig. 6 and is a strip detector as explained in section 2.3.3. The strips of the chip are connected to read out electronics leading to the read out connections at the right and left side.

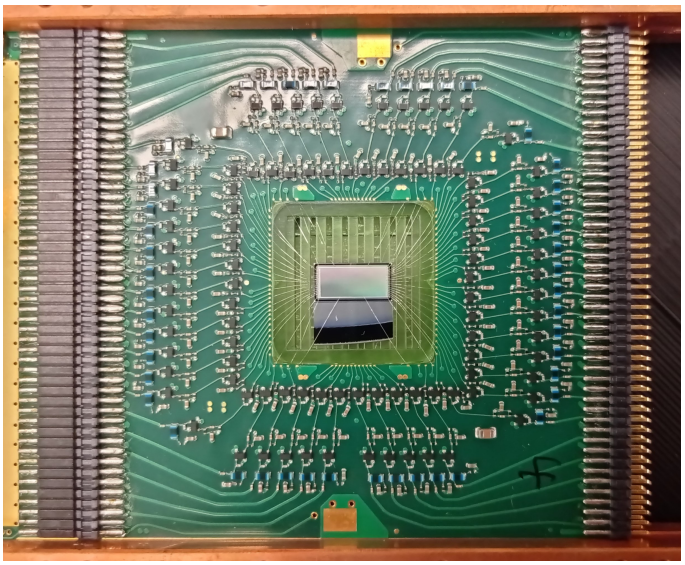

Figure 6: Picture of the LGAD silicon strip detector chip within the hardware.

The silicon strip detector chip, is connected to electronics, overall having 96 readout channels, which can be seen as 48 on the left and right respectively in fig. 6. The readout-channels are lined up on the edge of the detector and are alternating in their electrical polarisation. To connect the chip to the picoscope (SAMPIC), two adapters are necessary. The first adapter is presented in fig. 7 and the second is presented in fig. 8.
The first adapter is connected to 48 of the readout channels of the LGAD and separates the channels into 3 groups (batches) of 16 channels, which are marked in fig. 7. Henceforth, this group of 16 channels will be described as batches for an easier overview of the detector with the notation batch 1, 2 and 3 from left to right. The picoscope used, employs different wiring, requiring another adapter from output to Lemo cables, the second adapter can be seen in fig. 8.
The outputs have alternating polarisations, which for the readout has to be taken into account by the structure of the second adapter, switching the polarisation of every adjacent connection. This can be seen in fig. 8. Since only one side of the

LGAD is connected, the LGAD only has the first adapter for one side and cannot easily be moved, only the first 48 channels can be read out and only 18 of these channels are connected to the silicon chip. The connections are shown in table 1.

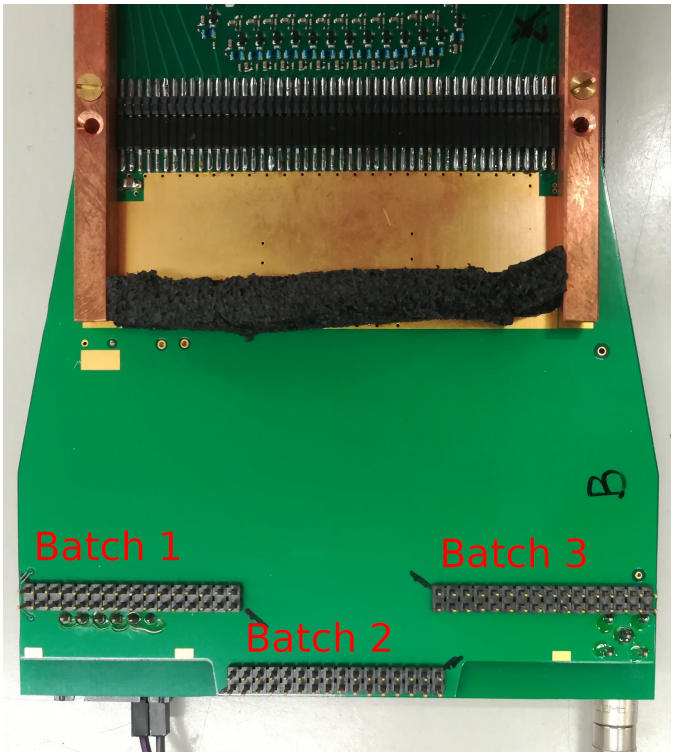

Figure 7: Picture of first adapter with markings of batch 1,2 and 3.

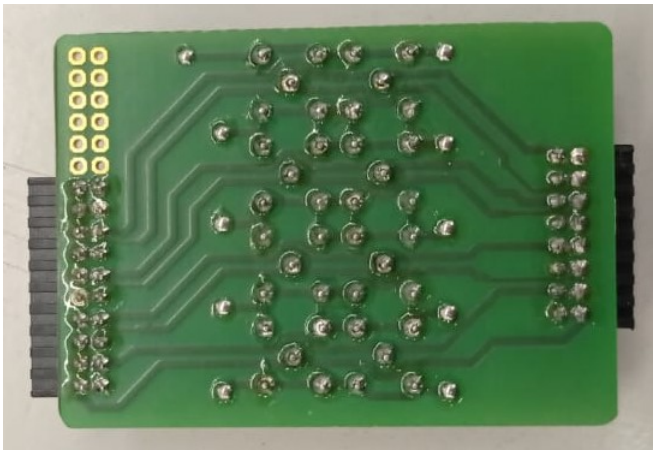

Figure 8: Pictures of adapter from signal to Lemo cable.

Channel	Batch-1	Batch-2	Batch-3
0	not	con.	con.
1	not	not	not
2	not	con.	con.
3	not	not	not
4	not	con.	con.
5	not	not	not
6	con.	not	con.
7	not	not	not
8	con.	con.	con.
9	not	not	not
10	con.	con.	not
11	not	not	not
12	con.	con.	not
13	not	not	not
14	con.	con.	not
15	not	not	not

Table 1: Table showing if the channel is connected or not, here shown as con. or not.

4. Methods, Results and Discussion

In this chapter, the methods and results for the experiments are described in detail, beginning with the measurement construction and a short introduction into the used picoscope (SAMPIC). Following this are the results for the noise measurements. In the end, rise time and energy resolution measurements are done with an $^{55}_{26}$Fe source. For the following analysis, the programming language python was used. The fittings of the measurements were done with the method of least squares.

4.1. Measurement Construction

The setup is shown in fig. 9. Additionally, to the devices already talked about in section 3, a high voltage source, seen in fig. 32 a low voltage source, seen in fig. 33 and the SAMPIC, seen in fig. 34 are needed. The LGAD, is being connected via two adapters and a cable to the SAMPIC and powered by the high voltage device at 160 V and a maximum of 15.0 μA for the avalanche process and a low voltage source for the drift current at 0.8 A at 1.4 V. The SAMPIC can then be connected to a PC with a USB cable, allowing for the readout and storage of signals. The

setup is shown in fig. 9 and all devices with exception to the high voltage source can be seen.

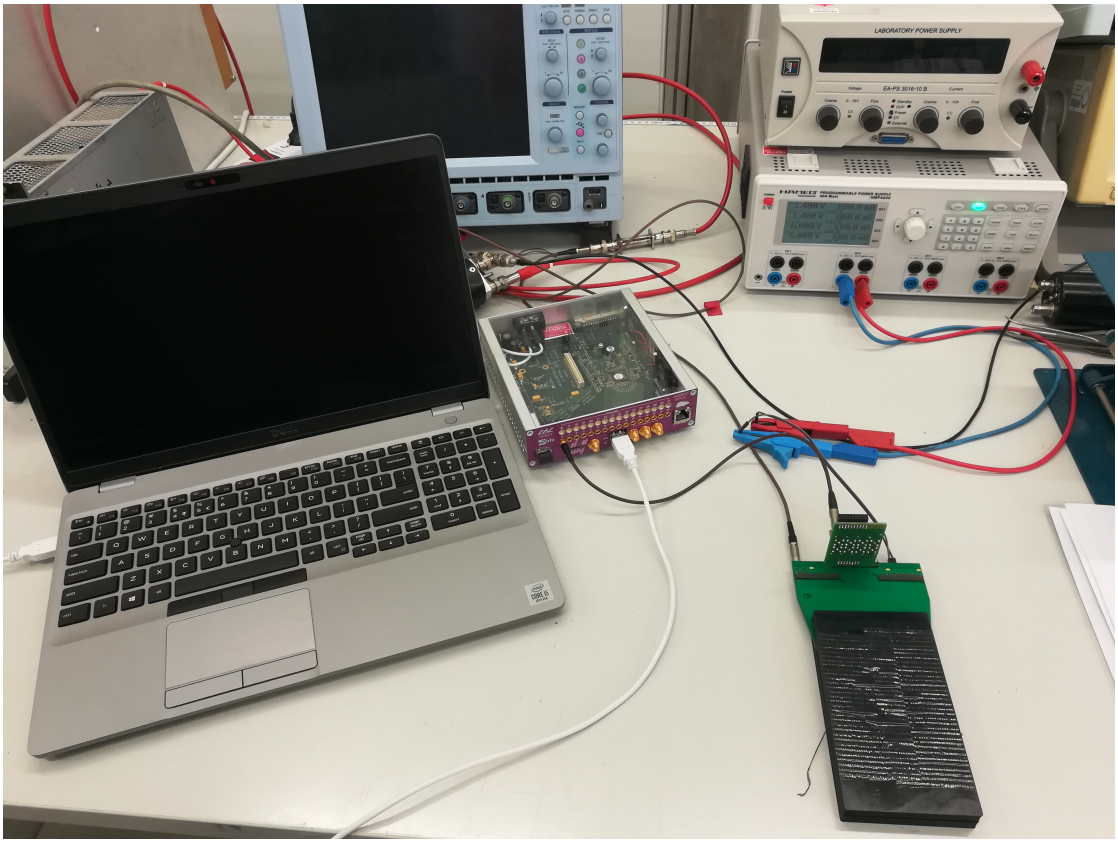

Figure 9: Picture of the setup with one channel connected.

4.2. SAMPIC

The SAMPIC (SAMpler for PICosecond time pick-off), which is a readout chip with picosecond resolution, used in the experiment has already been tried and tested by F. Ehring in his Bachelor thesis [Ehr22]. In addition, a converter written in python for the output file to easier use the data has been provided by F. Ehring, which was used and expanded in the following experiments.
The SAMPIC has a maximum of 16 connectable readout channels and a sampling frequency of 6.4 GHz. If the measurement of photon events is intended, the trigger is set to -0.010 V, to avoid minor noise to trigger the SAMPIC. Further used settings are shown for the software version 3.4.1 in fig. 35. Measurements are saved as 63 voltage measurements in 0.156 ns intervals, derived by the measurement frequency, over about 10 ns with an internally measured baseline value. The

internally measured baseline however is inaccurate as later a further correction is needed.
It was observed that the SAMPIC software has shown low stability when the LGAD itself showed problems. An example is a significant amount of noise signals, when the trigger is set too low. The source for this is unknown, but the problem is so infrequent that no influence is suspected for the results of the measurements made.

4.3. Noise measurement

For measurements of the noise of the available channels, a random trigger is used. This is achieved by setting the trigger level of the SAMPIC to 0. The measured data is collected in a histogram for each channel and can be fitted as a random distribution with a gaussian function. The standard deviation can then be calculated using the method of least squares. The equation employed for the gaussian fit is presented in eq. (6).

$$y = a \cdot e^{\frac{-(x-b)^2}{2c^2}} + d \tag{6}$$

It is unexpected that the last values of all signals seem to fall off at the end of the measurement, henceforth described as falling tail. While the reason for this is still unclear, using the results of F. Ehring [Ehr22], the SAMPIC can be ruled out as this was not seen in his results, implying an origin in the remaining part of the used setup. An example for a signal measurement is illustrated in fig. 10. While exceeding the scope of this thesis, further investigations into this behaviour are recommended.

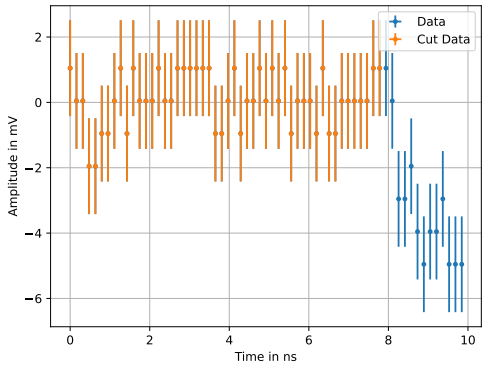

Figure 10: Measurement example of Signal with random trigger and falling tail. The data which is allocated to the tail is coloured blue, while the data with cut tail is coloured in orange.

Therefore, this leaves two possibilities to calculate the noise with a distribution.

One taking the falling tail into account and one not taking it into account, meaning to only utilizing the first 50 out of 63 measured points. Examples for these histograms for channel 0 of batch 1 can be seen in fig. 11. As seen in the examples below, an expected deviation to lower noise values can be observed when including the tail as described. However, cutting the tail, the originally expected Gaussian distribution for the noise, is achieved. As the tail influences the standard deviation, the actual uncertainty of the data points are taken as the sigma of the noise histograms with cut falling tail.

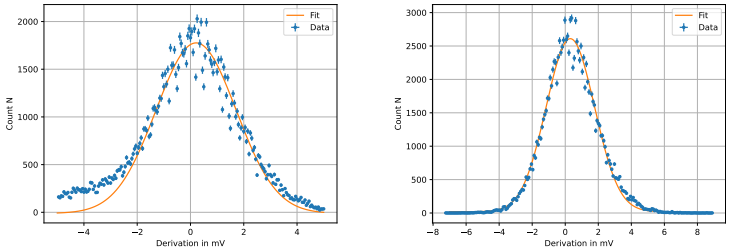

(a) With tail (b) With tail cut

Figure 11: Noise-histograms of channel 0 of batch 1 without and with tail-cutting. The results for these histograms are shown in table 2 and table 3.

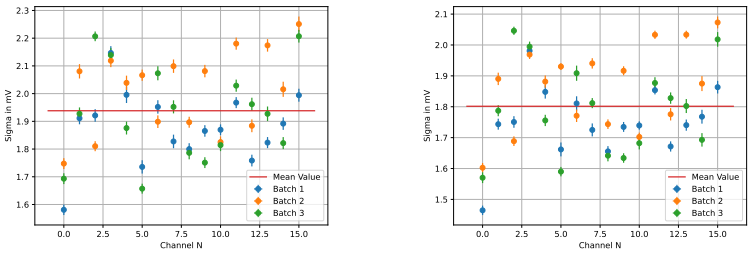

(a) Standard deviation σ for the noise of the Channels 0 to 15 for batch 1-3. The σ_{mean} was calculated as 1.938 mV $\pm$ 0.280 mV

(b) Standard deviation σ for the noise of each channel 0 to 15 for batch 1-3 with cut tail. The σ_{mean} was calculated as 1.802 mV $\pm$ 0.260 mV

Figure 12: Noise diagrams with and without tail cutting for all channels.

The example fits seen in fig. 11 have been done for each channel of each batch. The fits are all shown in appendix A.3. The results of the standard deviation with and without tail for each channel are visualised in fig. 42 and fig. 43, in fig. 12.

The difference between the results, with and without tail cutting, seems to only affect the overall amplitude of the noise. As while the amplitude of the distribution changed, the random distribution seems to have persisted. This is to be expected, as the falling tail would only create data with high deviation from the baseline and as such shifts the measurements to a higher average noise. This can be well observed when the structures of the datapoints of the signals with and without tail cutting are compared, as they show similar patterns. This is observed best in the mostly oscillating behaviour of batch 2.
It has to be noted that a slight deviation of the maximum from 0 was observed to higher values. While the origin is not known for certain, this might be explained by the fact that the measured data for the amplitude in the SAMPIC does only correct to the third decimal place, resulting in a rounding error in data taken with a random trigger. It is also possible that this effect has similar origin as the falling tail. However, as the baseline of the data is corrected in calculation of rise time and amplitude, as shown in section 4.5, it can be mostly ignored.
Overall, the noise does not seem to be correlated to the readout connection, however, this is only the case for channel 1 and 3 where the connected channels do still seem to create randomly distributed datapoints as expected. Nevertheless, batch 2 seems to show a clear oscillating behaviour overall, suggesting a correlation between connection to the silicon chip. It should be noted that for batch 2 channel 6 is not connected, which should result in channel 6 breaking or at least changing this behaviour. But as this outlying behaviour was only observed for channel 4 instead of the expected channel 6 and with batch 2 being an outlier in comparison to the other channels, no clear influence can be concluded for being connected to the readout. As such, it is implied that the noise largely originates in the electronics and not in the silicon chip, even in operation.
As shown in fig. 12, σ_{mean} can be calculated as $1.802\,\mathrm{mV} \pm 0.260\,\mathrm{mV}$ or when including the falling end of the signal as $1.938\,\mathrm{mV} \pm 0.280\,\mathrm{mV}$. The result for each channel individually are documented in table 2 and table 3. The distributions for calculation of the noise of each channel are as already meantioned presented in appendix A.3.

Channel	$\text{Noise}_{\text{Batch 1}}$ in mV	$\text{Noise}_{\text{Batch 2}}$ in mV	$\text{Noise}_{\text{Batch 3}}$ in mV
0	1.465± 0.015	1.602± 0.015	1.570± 0.017
1	1.744± 0.018	1.890± 0.020	1.787± 0.018
2	1.751± 0.019	1.689± 0.016	2.046± 0.013
3	1.981± 0.021	1.969± 0.014	1.995± 0.016
4	1.848± 0.022	1.881± 0.020	1.787± 0.018
5	1.662± 0.022	1.930± 0.011	1.590± 0.015
6	1.811± 0.023	1.771± 0.020	1.909± 0.025
7	1.725± 0.021	1.940± 0.017	1.812± 0.016
8	1.656± 0.017	1.744± 0.015	1.642± 0.018
9	1.735± 0.016	1.916± 0.015	1.634± 0.015
10	1.739± 0.013	1.702± 0.014	1.682± 0.020
11	1.854± 0.014	2.033± 0.013	1.877± 0.019
12	1.671± 0.017	1.776± 0.020	1.828± 0.018
13	1.740± 0.018	2.033± 0.013	1.802± 0.022
14	1.768± 0.022	1.875± 0.024	1.693± 0.022
15	1.863± 0.020	2.073± 0.019	2.018± 0.024

Table 2: Noise for each channel with cut tail.

Channel	$\text{Noise}_{\text{Batch 1}}$ in mV	$\text{Noise}_{\text{Batch 2}}$ in mV	$\text{Noise}_{\text{Batch 3}}$ in mV
0	1.581 ± 0.019	1.748 ± 0.020	1.693 ± 0.020
1	1.911 ± 0.021	2.080 ± 0.026	1.927 ± 0.022
2	1.921 ± 0.023	1.810 ± 0.018	2.207 ± 0.017
3	2.147 ± 0.024	2.119 ± 0.023	2.139 ± 0.025
4	1.996 ± 0.029	2.039 ± 0.026	1.876 ± 0.023
5	1.736 ± 0.024	2.066 ± 0.020	1.657 ± 0.018
6	1.952 ± 0.024	1.899 ± 0.023	2.073 ± 0.025
7	1.827 ± 0.024	2.099 ± 0.024	1.952 ± 0.024
8	1.800 ± 0.021	1.897 ± 0.020	1.786 ± 0.023
9	1.865 ± 0.021	2.081 ± 0.022	1.751 ± 0.020
10	1.870 ± 0.019	1.825 ± 0.020	1.814 ± 0.022
11	1.968 ± 0.020	2.180 ± 0.022	2.029 ± 0.022
12	1.759 ± 0.021	1.884 ± 0.023	1.962 ± 0.023
13	1.823 ± 0.020	2.174 ± 0.023	1.927 ± 0.026
14	1.892 ± 0.023	2.016 ± 0.027	1.821 ± 0.022
15	1.994 ± 0.023	2.251 ± 0.027	2.207 ± 0.023

Table 3: Noise for each channel without cut tail.

4.3.1. Nondominant forms of noise

While normal deviations only slightly influence the voltage values, other less dominant forms of noise are observed. One of these noise types has an oscillating form. An example is presented in fig. 13 and for ∼12000 measurements due to the trigger condition being fulfilled 0.083% are observed as these oscillating noise forms. With this low number in comparisons to the expected signals, the noise type itself is not considered to be a problem for the measurements. In addition, due to the way the signals are analysed, such false measurements are filtered out easily for the final results, in addition to the already mentioned low occurrence. The way this and later forms are filtered out will be discussed further below, as this is part of the rise time and energy resolution measurements. Therefore, influence of this noise type for the results are negligible.

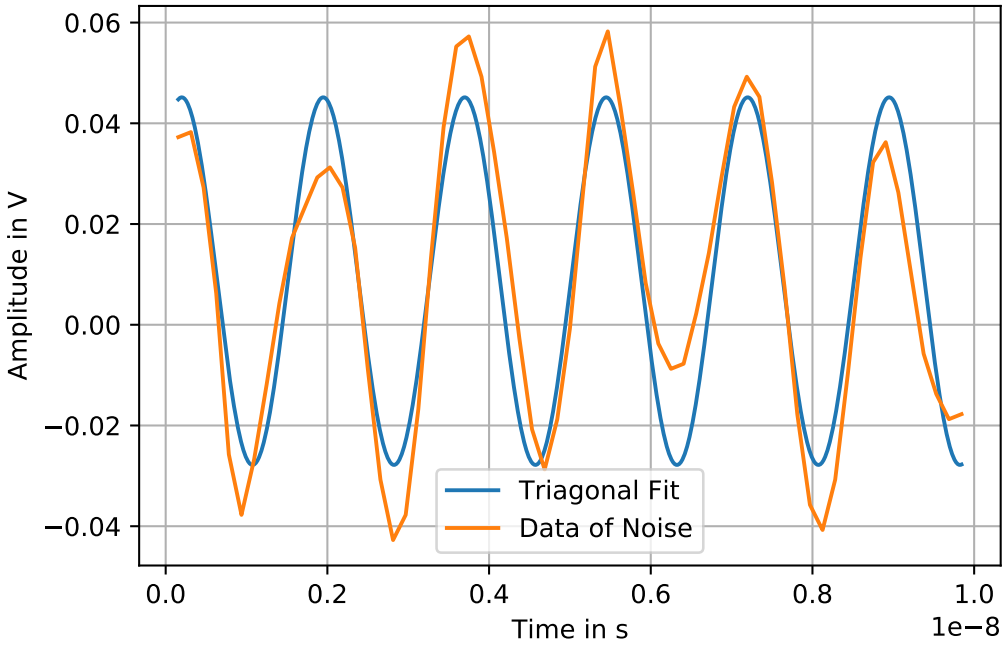

Figure 13: Diagram of the noise with a sinus fit to approximate the wavelength of the signal with a frequency $\omega \approx 3.6\,\mathrm{ns}$.

The origin of the noise is unknown, as the frequency of ≈3.6 ns, an example is presented in fig. 13, has no origin which it can be adjudged to. Suggested solutions are the power supply or more likely oscillations in the transistors of the electronics overall. In either case, as already noted, the event is considered to be irrelevant

for the following results.
Another form of noise is shown in fig. 14. For ∼12000 measurements due to the trigger condition being met, 0.017% are observed as this peak form, as such it is even rarer than the form before and filtered out. However, it shows a rather interesting form of a single measurement point being triggered. Especially with the rarity and the speed allocated to such a measurement, it is expected to originate in the readout software of the SAMPIC or LGAD. A more detailed investigation into the origin of this event type could show interesting results. Nevertheless, such action is not necessary, as the readout is not vastly influenced due to this kind of event being easily filtered out and in addition having a low statistical appearance.

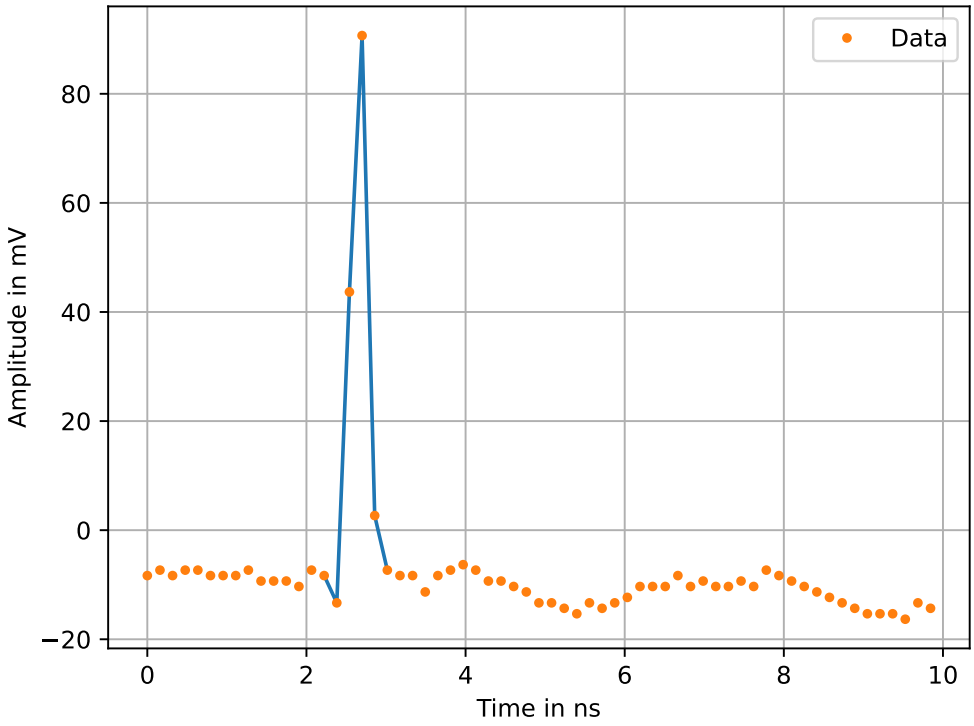

Figure 14: Triggered point like sample of an unexpected kind of signal with uncertain origin.

Another form of noise with unknown origin could be found when looking at the channels 0, 2 and 4 of batch 2 with examples presented in fig. 15. This specific kind of signal could not be observed for any of the other channels and could give a hint to the different performances. In contrast to the other channels, when

calculating the rise time and the energy resolution, rather large deviations are observed. Again however, of ≈ 34000 signals only 1.089% are these noise forms. As such, they do not appear often and can easily be filtered out and discarded so they do not influence the results.

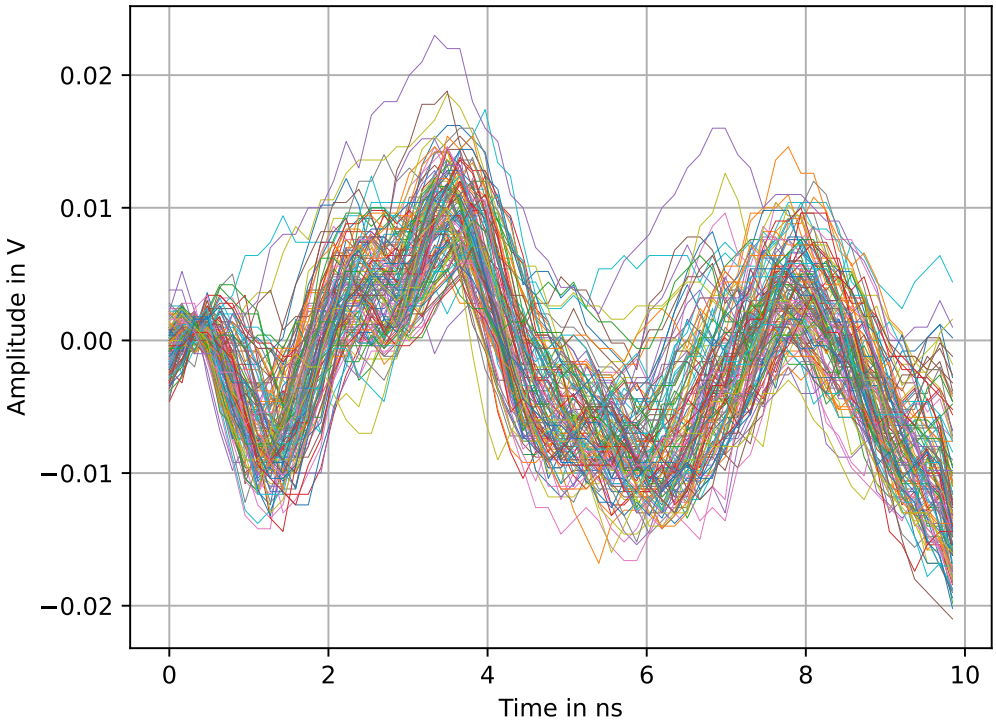

Figure 15: Signals as seen in batch 2 with unknown origin.

Curious for this kind of signal is not only their frequent appearance but also their similar form. It is to be expected that these channels have been damaged in the earlier measurement process, as these were only noticed in later measurements. An investigation into this problem is recommended, as the active prevention of such damages or problems would certainly be helpful for experiments using this detector.

4.4. Experiments searching for Cosmics

To start the experiments, for detection of particles, the LGAD was used to detect cosmic particles such as myons. In addition, the high energy deposited into the

detector was used to check if charge sharing was present. However, due to the low cross-section of the silicon detector, not enough events could be captured to give statistically representable results in a reasonable timeframe for a bachelor thesis. Nevertheless, in minuscule amounts, cosmics were observed in measurements. In some cases, when measurements with a different source are made, a detection of a cosmic with vastly higher amplitudes were observed. These events were so rare however that even without filtering, the influence was in no case notable to the measurements. An example of an event can be observed in fig. 16.

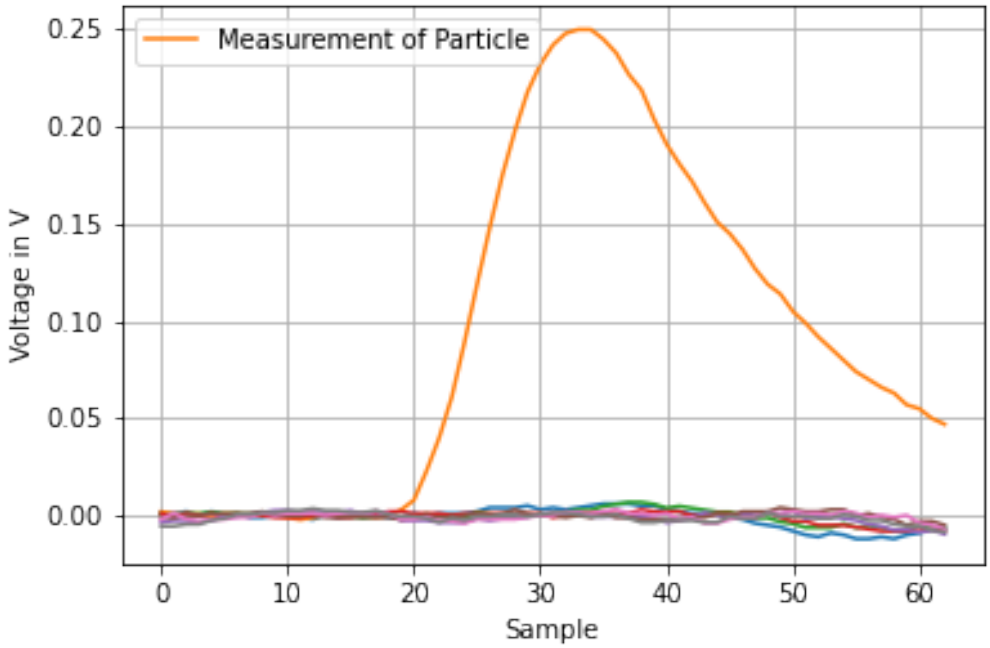

Figure 16: Example measurement of a cosmic. With all neighbouring channels shown additionally for investigations into charge sharing.

It could be seen here that charge sharing as explained in section 2.3.3 was not present, as the signals of the cosmics do deposit a lot of energy and should be in this case distributed over the two neighbouring channels. As already seen in section 3, no adjacent channels are connected, as such making the observation if charge sharing is present or not impossible, as only sharing with neighbouring channels in silicon-strip-detectors is expected.

4.5. Investigations into rise time and energy resolution

To measure the rise time and the energy resolution of the LGAD, a signal source was needed. Due to availability and the known energy of the electrons emitted by the beta-decay in $^{55}_{26}$Fe, the source used had an activity of 5.1 MBq (last checked: 08.06.2020). $^{55}_{26}$Fe decays in an electron capture process emitting photons with an energy of 5.89 keV, 5.96 keV and 6.49 keV [Sch00], resulting in an observable energy difference. As such, particle detectors with a good energy resolution would observe a double peak. The LGAD is primarily dedicated for use in spatial and temporal resolution, since the energy resolution is not expected to be good enough.

4.5.1. Rise time

For the calculation of the rise time, events, meaning the measurement of a photon depositing energy into a detector, originating from the $^{55}_{26}$Fe source, were measured. To measure the events detected by the LGAD, the SAMPIC was used, which was introduced in section 4.2. However, it should be noted that the deposited energy of the $^{55}_{26}$Fe photons is quite low, resulting in the signal-to-noise ratio to be far lower in comparison with the earlier shown events of cosmics in fig. 16.

Fitting with Quadratic functions The signals from start to peak were fitted using Matplotlib with a quadratic function as presented in eq. (7).

$$y = ax^2 + bx + c \tag{7}$$

A quadratic function was chosen, as it describes the rising area well with a low deviation as seen in the example of fig. 17, while not taking the falling edge into account. This is justified if the only aim is the calculation of the rise time. For a program which analyses event signals systematically, this will lead to problems as described below.

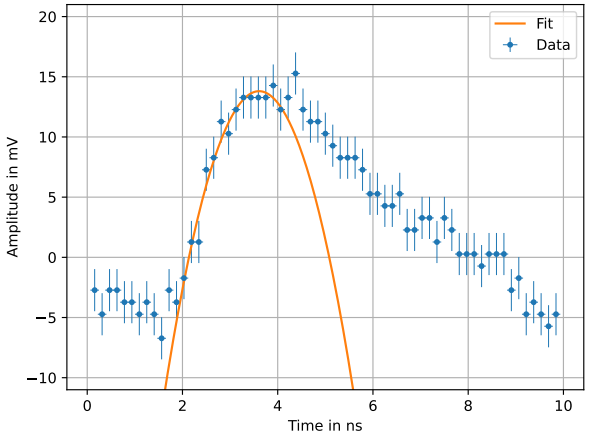

Figure 17: Example of an $^{55}_{26}$Fe event with quadratic fit for the rise of the function, as described with eq. (7).

The rise time was then measured as the time which is needed for the signal to increase from 10% to 90% of the maximum amplitude. By using this description of the rise time, it is necessary that the amplitude of the voltage before receiving a signal, called the baseline, is at zero. Since the baseline measured by the SAMPIC is not always at zero, a correction is made by subtracting the signal with the mean of the first 5 data points of itself. The baselines corrected by this simple method show good results and as such good distributions for the rise time.
As the signal-to-noise ratio for the low energy photons is not high, applying a fitting program proved to be difficult, as the energy deposited by the photons was not constant. Partially high fluctuations of the signals created deviations, making the setting of starting parameters for the quadratic fit difficult. This problem was amplified by the small amount of datapoints used for the fitting process, as only the rising edge was taken into account. The starting values for y- and x-values of the peak are represented with the constants b and c in eq. (7). They can be found by using the coordinates of the highest datapoint of the measured signal. Here, a difficulty for the fits was found, as the highest datapoint could be largely influenced by noise, creating an artificial shift of the maximum present in the signals. This problem could not sufficiently be fixed by using the quadratic function and will be solved with a better approximation of the signals as described later. It is also to be said that small deviations from the starting values for the fitting function excessively influenced the accurate description of the rising edge of the signal.
While the earlier mentioned constants can be sufficiently found with the maximum of the signal, the parameter a turned out to be more complicated to find. This

means that if the value was too big, fitting could not be accurately achieved, especially with some of the signals keeping a maximum at high level for a longer time than expected, resulting in a smearing out of the fit functions and a high constant a and in direct result also a higher rise time as actually present.
To minimize the influence of the noise for the areas effected, in the beginning the edges were partially cut if the calculated fit was not within 1 ns of the x position and within 3 mV of the actual maximum of the signal, given as the highest value of the data. As this was deemed as inaccurate representation and vulnerable to more excessive noise of the data, this was replaced with data point corrections taking the uncertainties of the fit values into account, as a miscalculated maxima or inaccurate fit of the rising edge leads to high uncertainties of the fit of least squares. This correction could later be disregarded, as the more accurate description of the signal form with the exponential function did not need such support to accurately fit the signal. Also, if too few data was determined by the program due to cutting, more were added to give the possibility of a fit the inverse way data was cut.
While the overall few data are expected to create rather inaccurate fits, those adjustments seemed to help fit more noisy functions and were not needed in better functions, resulting in overall better results. To not influence the results by discarding too many inaccurate results, the process was often repeated until only an insignificant number of signals (about 1% or less), which were not part of the noise found and described in section 4.3, were taken as too inaccurate.
To look for a correlation between amplitude and rise time, scatterplotts with density-colour-coding have been made. One example is presented in fig. 18. In addition, the density-distributions were useful for error hunting, as the rise time and amplitude are connected in the method for calculation due to using the same fits. Problems could often be individual, resulting for example in doubling of intensity centers, or only one dimensional deviations in the diagrams, which could be seen by showing problems for one kind of fits.
As visible in fig. 18, the rise time and the amplitude do not appear to have a correlation but more distinct results with a smearing out to higher rise time and lower amplitude. As the already mentioned problems made the analysis difficult, the such found results will not be further discussed using the quadratic function and will rather be discussed later in the use of the exponential function.

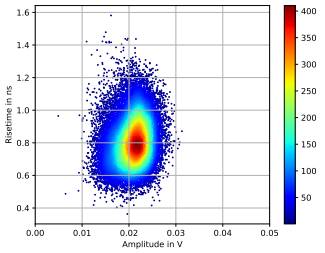

Figure 18: Example of a scatterplot of the amplitude to the measured rise time. The considered channel here is channel 10 of batch 1.

Additionally, one should note that with the program for the rise time function, it is also easy to find noise forms, which were already discussed in section 4.3. The reason for this is that the amplitude and the parameter a for fits strongly deviates from the other results of a measurement, as the fitting function is not suited for such events. This benefit will further be carried on into the new fitting program, as it poses a modification of the original way in which a signal was quadratically fitted.

Fitting with exponential functions To fix the already mentioned problems, another fitting function was needed. In addition, it was expected that a more accurate description of the signal would simplify the fitting methods which earlier required a heavy workload for each individual channel, as the starting parameters for each one have to be accurate to wield good results. The following function was taken from [Col18]:

$$y = \frac{a}{b}(x - c)e^{-\frac{x-c}{b}} + d \tag{8}$$

An example of the fit made with this new function is shown in fig. 19. Datapoints which can be used for the fit are shown in orange and must be distinguished from the earlier datapoints which are not represented in the fitting function. As this was already needed for the quadratic fit, the first created program for the quadratic fit could be modified. In case of a quadratic fit function, the data points were only fitted until the maximum of the function or slightly further for accuracy. Using the whole tail resulted in a more reliable fit. Due to the majority of the used data being behind the maximum, this part of the function could be fitted more accurately by using the method of least squares. For low amplitudes or noisy signals, not using the full rising edge, resulted in difficulties to accurately fit and as such in problems for the rise time distributions. To reliably find the first datapoint to use, the sharp rise and the calculated rise time of about 1 ns, which has already been calculated with the quadratic functions earlier, are exploited. To find the start of the rising edge, each datapoint was checked with a condition of being above 10% of the

maximum amplitude measured and a condition of the next 3 datapoints to be of a higher amplitude than each of their individual previous. The first instant the condition was achieved was taken as the beginning of the rising edge. While this idea seemed simple, it showed great effect for the then created fits and rise time distributions calculated. The correction for the baseline also in use here, showed sufficient results.
The function resulted in more accurate depictions of the signals overall, as seen in fig. 19, which used the same signal shown before in the example for the quadratic method.

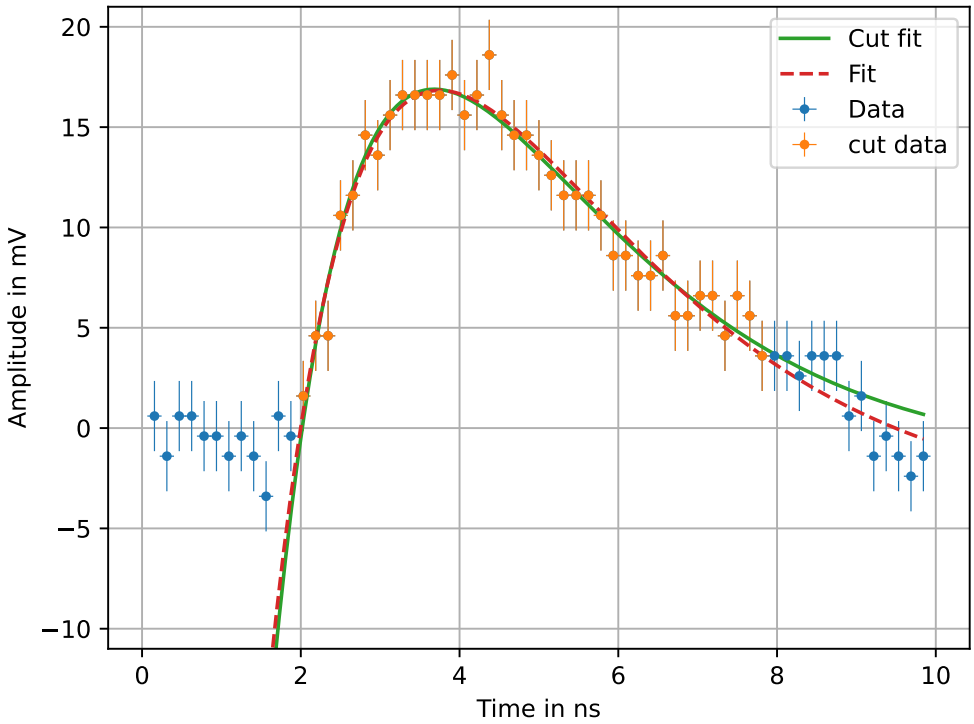

Figure 19: Representation of an example measurement with and without cut data. The orange datapoints were determined to be used for the cut fit with eq. (8).

As seen in fig. 19, the falling edge of the baseline, as already noticed in calculations of the noise, can be observed here again. This results in a lowering of the measured values below the baseline. This is questionable to analyze as such behaviour should not appear as the voltage should just return to the baseline. Therefore, as already done for measuring the noise, a cut off at the 50th datapoint is used, resulting in

the representation of the data seen in fig. 19. However, it can be observed that fitting in this way partially impacted the rise time both positively and partially negatively depending on the channels. For some channels, like channel 0 of batch 2, the results were only partially better. And for example channel 10 of batch 2 they worsened. Examples of this behaviour are shown in fig. 20. This is seen well, in channel 0 of batch 2 as the cut distribution can be fitted well with a gaussian function, while the uncut distribution shows a larger deviation to higher values and a larger smearing out to smaller values, all in all positively influencing the distribution when the values are cut. In contrast, channel 10 of batch 2 show a tightening of the lower values while not making on the higher values. In both cases, the rise time also shifted as the peak is moved. All in all, cutting did not seem to have a great effect and created problems for some channels while wielding no clear advantage. Therefore, and also not to overestimate the rise time, it was decided not to be employed, as the signal could still be fit well without cutting as seen in fig. 19.

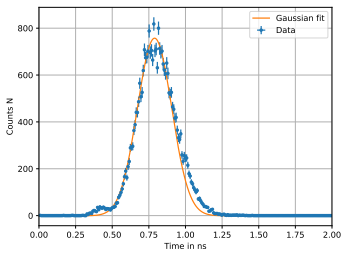

(a) Rise time distributions for channel 0 batch 2 cut

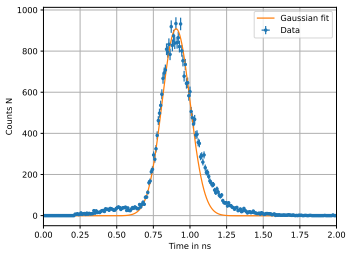

(b) Rise time distributions for channel 0 batch 2 uncut

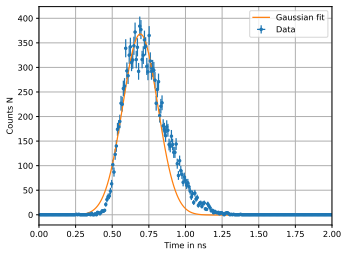

(c) Rise time distributions for channel 10 batch 2 cut

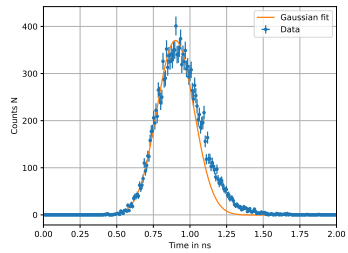

(d) Rise time distributions for channel 10 batch 2 uncut

Figure 20: Representation of positive and negative effects by cutting in calculation of the rise time. The channels taken for the examples are channel 0 and 10 of batch 2, respectively.

Results for rise time measurements The results for the rise time histograms, as seen in the uncut examples of fig. 20, still have a slight deviation of the gaussian distribution to higher rise times. The reason for such behaviour is unclear, especially as this is observed in different intensities. The peak or rather the result for the overall rise time is calculated with a gaussian function. However, the deviations are not taken into consideration as the fit will be influenced, resulting in inaccurate results for the majority of signals. This is the reason why the deviating edges of the histograms are not taken into consideration for the gaussian fits. The results are shown in table 4 and for comparison in fig. 21. Most results agree with the average value within their given uncertainty. All values agree within 2 σ of the average value. The deviation cannot be clearly dedicated to a cause, but is fairly accurate anyhow. The fastest channels here seem to be channel 0, 2, 4 and 14 of batch 2, however this could be in connection to problems later discovered in section 4.5.2, an investigation is suggested due to the faster rise time in connection to the other channels. Overall, the average rise time can be calculated as 0.964 ns $\pm$ 0.234 ns, which is very fast as expected and intended for silicon detectors.

Channel	Batch-1 in ns	Batch-2 in ns	Batch-3 in ns
0	not	0.863±0.079	0.996±0.156
1	not	not	not
2	not	0.850±0.073	0.996±0.146
3	not	not	not
4	not	0.867±0.073	1.051±0.141
5	not	not	not
6	1.044±0.122	not	1.136±0.178
7	not	not	not
8	1.010±0.150	0.939±0.142	1.081±0.122
9	not	not	not
10	0.964±0.112	0.909±0.135	not
11	not	not	not
12	1.003±0.127	0.914±0.137	not
13	not	not	not
14	0.917±0.103	0.856±0.119	not
15	not	not	not

Table 4: Table showing the rise time of each connected channel as calculated in the histograms of fig. 40.

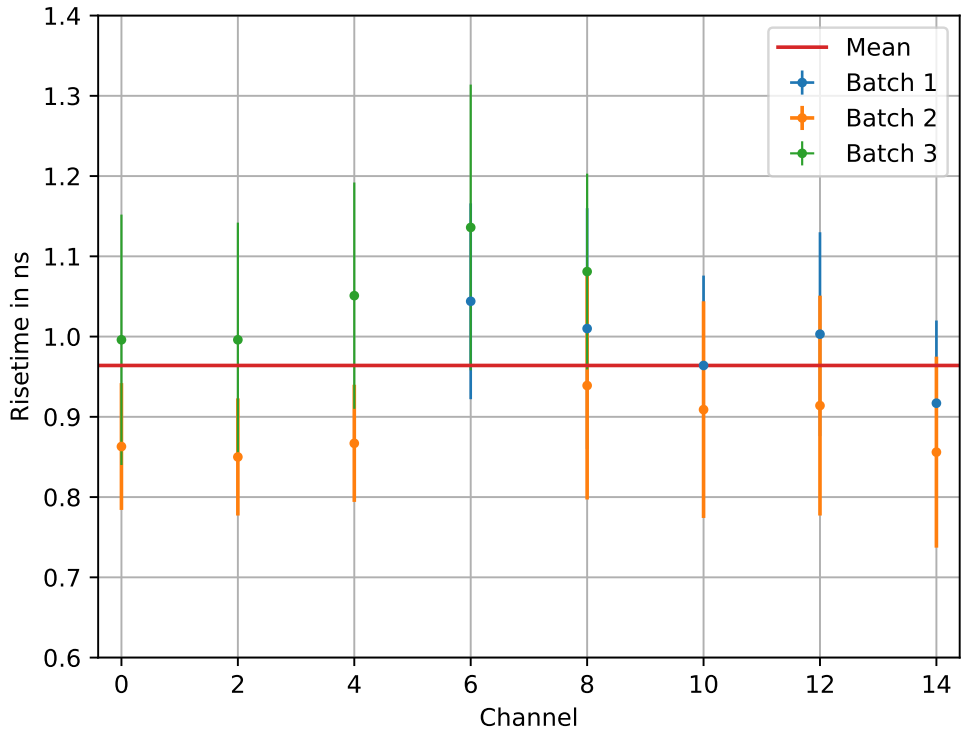

Figure 21: Results for the rise time of the connected channels for Batch 1-3.

4.5.2. Energy resolution

To measure the energy resolution of the LGAD, events from an $^{55}_{26}$Fe source are being detected. The photons emitted have three energies, with 5.89 keV, 5.96 keV and 6.49 keV [Sch00]. As the energy difference between the photons of 5.89 keV and 5.96 keV is miniscule and the LGADs primary purpose is not to measure energy, those two different photons are henceforth treated as the combined peak of 5.9 keV, as distinguishing between them is not possible for the detector. The measured voltage peak should be dependent on the deposited energy of the particles, allowing for energy measurements of the detected events. Using an X-ray source like $^{55}_{26}$Fe is especially useful, as the peaks created by photons are very sharp due to the way energy is deposited by photons (see: section 2.2.1).
The easiest way to find the peak is to use the maximum of the measured signals. However, it is disregarding the rather low signal-to-noise ratio, which can have high influences on the amplitude. It is already obvious in the earlier fig. 17, that using the maxima of the signal will likely result in a positive shift of the amplitude

due to noise. As the calculation of the rise time included a fit of the maximum of the signal, the peak position could be calculated using the results of the used fitting program. Therefore, it was tested if the amplitude calculated is usable for the calculation of the energy resolution either with the quadratic or the exponential fit.

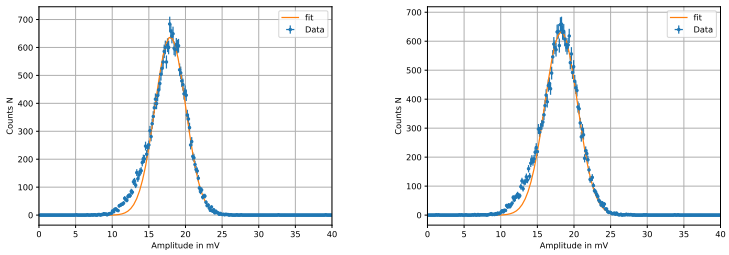

(a) Exponential fit of the rise time function 17.928 mV ±2.103 mV

(b) Quadratic Fit of the rise time 18.257 mV±2.236 mV

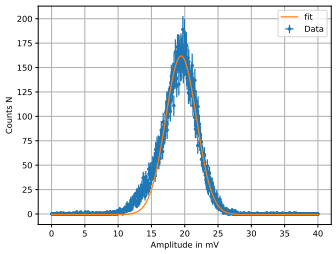

(c) Maximum of the Signal Fit 19.455 mV±2.318 mV

Figure 22: Amplitude distributions for the maxima of data taken by channel 12 of batch 1. The different methods of determination of the peak position are shown in an individual diagram.

As observed in fig. 22 the different methods for calculation of the amplitude yield different results. While the calculation with the exponential and the quadratic fit seem to have a similar result, calculation using the maximum of the signal, presented in subfigure c), only seem to have a result with higher amplitude. However, it is to be said that within the scope of uncertainty, the results are consistent. Looking at the distribution result for signal maxima in the example, as expected, taking the influence of the noise into account, the results show a deviation of ≈1.2 mV and ≈1.5 mV respectively to the results calculated by the fits which are less influenced by noise as seen in subfigure a) with the exponential fit and seen in subfigure b)

with the quadratic fit. This is expected, as the maxima which are found this way are heavily influenced by the noise in the channels which, as mentioned before, is quite high compared to the signal itself. Taking only the highest signal as peak position into consideration is thereby not accurate and will further not be used again.
Comparing the exponential and the quadratic fits resulting histograms, not much of a difference is being seen, with results only differentiating for ≈0.3 mV. As seen in fig. 23, both methods come to a good result for the maximum. To get good results for the calculation of the energy resolution, precision should be as high as possible, requiring as many datapoints as possible. The exponential function uses many more datapoints than the quadratic, as it also describes the falling edge of the signal and not just the rising edge. Therefore, the exponential fit is considered to have a higher accuracy and as such was decided to henceforth be used.

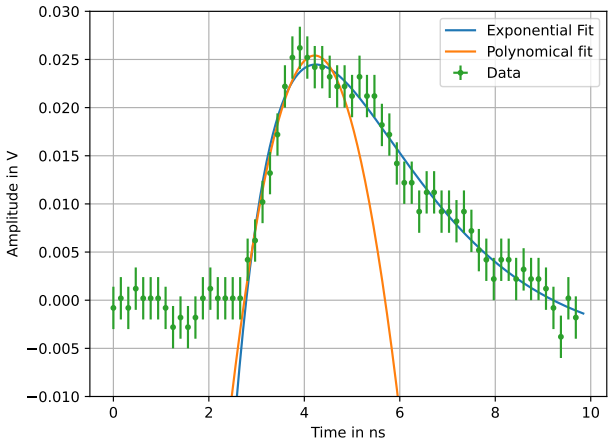

Figure 23: Example fit for a signal of channel 0 of batch 2 with quadratic and exponential method in direct comparison.

The noise signals and any other problems already encountered in the rise time calculation as seen in section 4.5.1 are here also being taken into consideration.
The amplitude distributions, an example is presented in fig. 24, show a deviation to lower average energies measured for the particles. This deviation from the Gaussian distribution is possibly caused by electron-hole-pair creation in a weak electronic field resulting in recombination of charges and such in a lower measured energy of the detected particles. Another possibility, the influence of another photon peak emitted by the $^{55}_{26}$Fe source, should not be the reason, as a lower energy X-ray than the typically seen 5.9 keV does exist, but as already said the

difference of the peaks is a miniscule <0.02 keV and as the X-ray with ≈6.5 keV which is also emitted by $^{55}_{26}$Fe can not be seen as a separate peak, the resolution should not be high enough to show a significant shift. This argument can further be seen in fig. 31, where the 6.49 keV, 5.89 keV and 5.96 keV peak is shown.

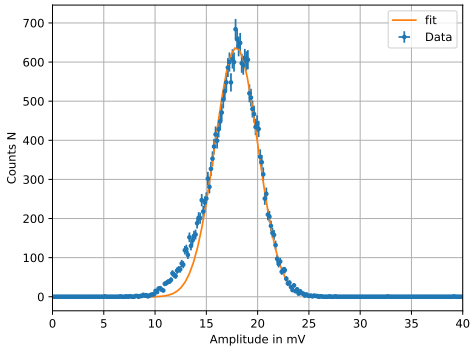

Figure 24: Amplitude distributions for the maxima of data taken by channel 12 of batch 1. An exponential fit function was used and a σ of 17.928 mV ±2.103 mV was calculated.

To avoid influence of parts deviating from the gaussian distribution to the measurement, parts making up the vast minority of the distributions were neglected for the calculations to accurately fit the majority of values. It is to be of note, however, that not all channels needed this correction, as the influence of the deviation on the results vastly varied.
The results of the measurements are shown in table 5 and the histograms used for the calculations are depicted in fig. 41. In addition, for an easier discussion, the results are all represented in fig. 29.
Channels 0, 2 and 4 of batch 2 and channel 8 of batch 1 show an unexpected behaviour in the form of a second peak forming separately from the expected peak allocated to the expected photons. The second peak consists of events with a different signal form, presented in fig. 25. The second peak can be seen best in channel 8 of batch 1 for example fig. 26 a).

Channel	Batch-1 in mV	Batch-2 in mV	Batch-3 in mV
0	not	25.713±3.431	16.364±2.009
1	not	not	not
2	not	26.808±3.800	17.014±2.129
3	not	not	not
4	not	29.377±1.871	18.745±2.208
5	not	not	not
6	20.356±2.028	not	19.135±2.068
7	not	not	not
8	21.634±2.246	16.337±1.871	22.695±1.795
9	not	not	not
10	21.583±2.237	16.946±2.248	not
11	not	not	not
12	17.928±2.103	18.932±1.949	not
13	not	not	not
14	19.561±1.934	19.135±2.068	not
15	not	not	not

Table 5: Table showing the amplitude of each connected channel as calculated in the histograms of fig. 41.

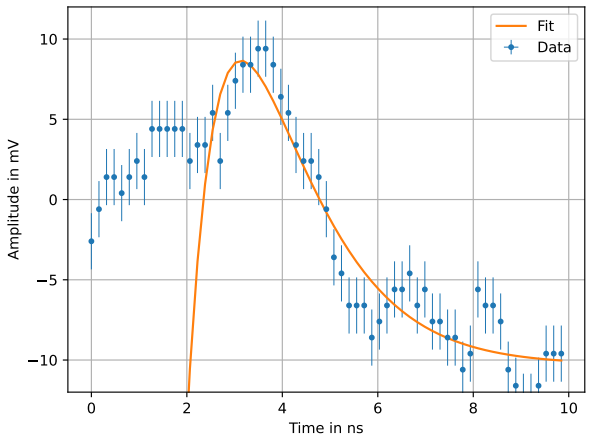

Figure 25: Signal observed for the second peak by channel 8 of batch 1.

It can be observed that a vast part of the signal is positioned below the baseline. As this is so dominant in the signals, it cannot be allocated to the already present and expected falling edge of the baseline talked about in section 4.3. Additionally,

before the rising edge, the amplitude is above the expected baseline. Lastly, the peaks as seen in the distributions presented in fig. 26 show a deviation from the originally expected amplitude, as if a particle of second energy is seen. This however is impossible as other channels would have also observed this.
As only these four channels show the presence of this signal and the second peak, it is likely that the peaks share a similar origin. To investigate this, it has to be taken into consideration that the channels differ in the amplification of energy deposited into them, making it necessary to convert the amplitude into keV. The conversionfactor necessary for the conversion is explained later. This is done in fig. 26 b) and d) for channel 8 of batch 1 and channel 4 of batch 2.

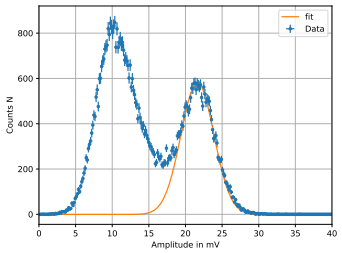

(a) Channel 8 of batch 1 with unexpected second peak in mV.

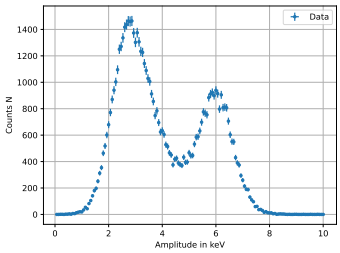

(b) Channel 8 of batch 1 with unexpected second peak in keV.

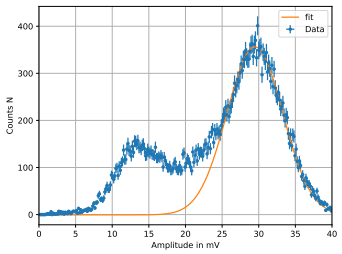

(c) Channel 4 of batch 2 with unexpected second peak in mV.

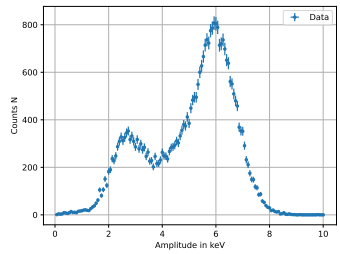

(d) Channel 4 of batch 2 with unexpected second peak in keV

Figure 26: Example distributions for measured Amplitudes with second peaks.

If fig. 26 b) and d) are compared, the second peak shows the same amplitude in keV in both cases, hinting for a similar origin of the problem. While not known for certain, the problem is expected to originate from a malfunction of the electronics. This is reasoned with the fact that the baseline does not return to 0 after detection or before a new signal, even when taking the intrinsic falling edge in the measurement into consideration, as it can be observed for the example in fig. 25.

This observation can be seen well when correlations between the amplitude and the baseline correction, described as amplitude deviation, are shown in a density distribution diagram. This is visible in fig. 27 b) with the rise time against amplitude deviation.

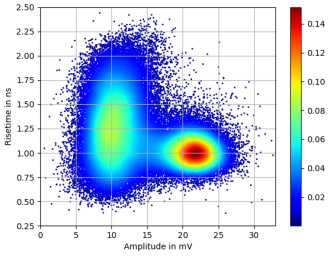

(a) Density risetime amplitude distribution for channel 8 of batch 1

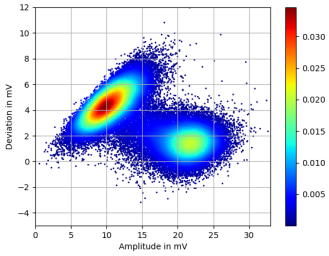

(b) Density Amplitude deviation distribution for channel 8 of batch 1

Figure 27: Colourcoded scatterplot diagrams amplitude against deviation. The data belonging to channel 8 of batch 1 is shown.

Nevertheless, the amplification itself seems to be working fine, as it is visible that the amplitude taking the amplification into consideration seems to be fine. At least channel 8 shows a reasonable value for the amplitude of the detected particle, as observed well in fig. 29.
What also has been of note for the double peak is a change in detection rate over time. However, this behaviour was not observed in any other channel than channel 8 of batch 1. This is clearly visible in the distributions of fig. 28 showing the first 16000 calculated amplitudes in 8000 datapoint steps.
More continued measurements over time are presented in fig. 38. The origin of these phenomena is unknown. As the other channels do not show the second peak, a comparison of the detection rates is difficult. To investigate any changing effects, channel 10 of batch 1 was tested in 4000 datapoint steps. No changes could be observed. The results are presented in fig. 39. As the whole measurement was made with en exposition time of 15 min, the first diagrams show a change in amplitudes over minutes, with each 8000 steps taking more than a minute. Overall, it is to be expected that a part of the electronics has been damaged, while no concrete proof or origin can be determined.

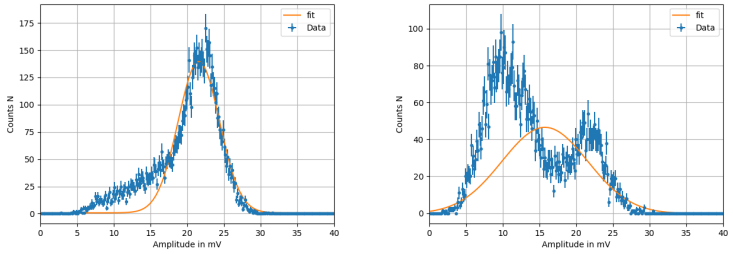

(a) Distribution of the calculated amplitude for the first 8000 signals.

(b) Distribution of the calculated amplitude for the 8000th to 16000 signals.

Figure 28: The first two 8000 datapoint distributions over time from channel 8 of batch 1.

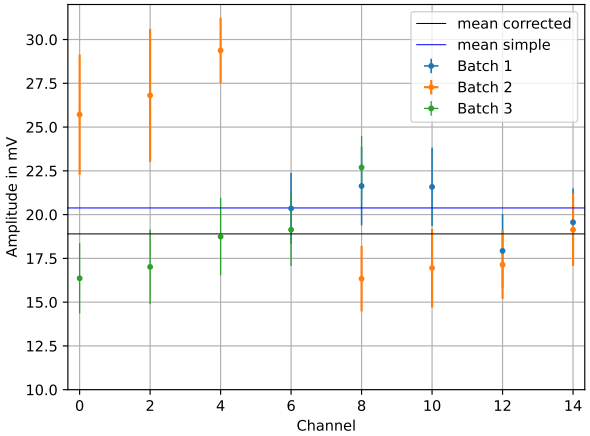

Figure 29: Diagram of the amplitudes in mV for all active channels and a mean value with and without the questionable results of channels 0,2 and 4 of batch 2. The mean values calculated are 20.381 mV and further corrected 18.898 mV.

As seen in fig. 29, most channels do seem to be around the calculated mean value for the amplitude, ≈19 mV. Still, a few exceptions are seen deviating over more than one σ. This is most extreme in the already talked about channels 0,2 and 4 of batch 2. As the vast deviations from the mean values are unexpected, it is suspected that a problem with the measurement process is seen. Therefore, these values are not used for calculating the mean amplitude in the following discussion. The origin of this problem is unknown, but is suspected to be allocated in the

electronics. It is possible that the higher amplitude is in connection to the second peak observed earlier, as these are the affected channels. However, since channel 8 of batch 1 also shows this second peak but does not deviate that much from the mean, it is not assumed to be related. At this point it is to be said that at one measurement only channels 0-7 and 8-15 could be measured due to the experiment's limitations. Thereby, it is also possible that, as these three mean amplitudes were taken in one measurement independent of the other channels, the measurement itself had problems. Following this assumption, it is possible that additional lighting from normal lamps influenced the amplitude. This was observed in earlier measurements and taken into account later, as such it is unlikely but would explain the higher amplitude.
It was also observed that a rising amplitude in batch 2 and 3 with rising channel number of each measurement, as visible in fig. 29. It is unknown what causes this rising behaviour. As this should not be caused by the radiation, the origin is suspected to be in the used hardware, or it could be a statistical occurrence. As the behaviour does not seem to be symmetrical, it is to be expected that the LGAD sensor itself is not part of the problem, so a probable origin could be the adapter used to connect to the SAMPIC sensor.
Another suggestion for the problem would be pressure on the adapter, which was present in the measurements due to the cables being mechanically static when bend as needed for the construction. A result was a slight tilt of the adapter. It is possible, therefore, that the contacts were not fitting well, resulting in contact resistance in the direction of the tilt. This would be amplified due to the weight of the adapter and connecting cables. However, this would imply the values of 0 and 8 to be the most accurate, as they are at the well sitting edge of the readout considering the two measurements needed for the readout of 16 channels, which is unlikely as the values of channel 8 and 0 differ vastly. Thus batch 1 behaves vastly different, implying another problem.
The energy of the photons emitted by the $^{55}_{26}$Fe source are at about 5.9 keV, as the voltage of the signal corresponds linearly with the amplification of the signal. Therefore, using the amplitudes already found in section 4.5.2, it is possible to adjust to energy in keV. To calculate the factor a from voltage to keV, the formula presented in eq. (9) can be used to calculate the voltage to the deposited energy.

$$a = \frac{U_{Peak}}{5.9\,\mathrm{keV}} \tag{9}$$

The results for each channel are shown in fig. 30. The σ of the results for the energy calibration can now be used to determine the resolution of each channel in mV for the readout and in eV and % for further use. The results are shown in fig. 30 and additionally presented in table 6 and table 7.

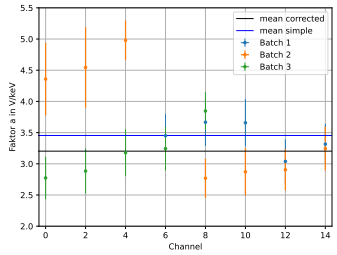

(a) Conversionfactors from detected Voltage to energy for each channel.

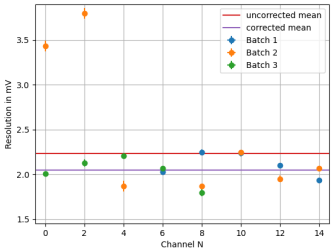

(b) Amplitude resolution in mV for all connected channels.

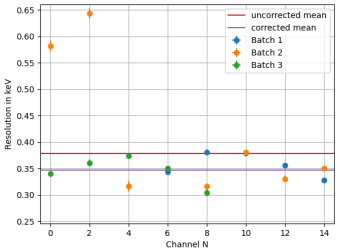

(c) Energy resolution in keV for all connected channels.

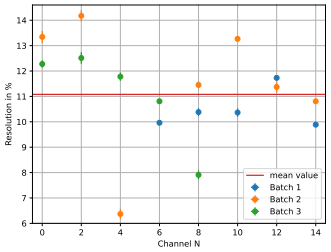

(d) Energy resolution in % for all connected channels.

Figure 30: Diagrams for different presentations of the energy resolution, in mV b), in keV in c) and in % in d) and the conversionfaktor a).

Using the results, it can be easily shown why a double peak is not seen in the results. An example with lines for the three peaks calculated are shown in fig. 31. It is to be of note that the peaks were deduced with the method described above, resulting in a slight shift to higher amplitudes and a slightly broader distance between the peak positions. Keeping this in mind, in the now used method it can already be seen that a distinction between the peaks with the energy resolution as it is not be achieved.

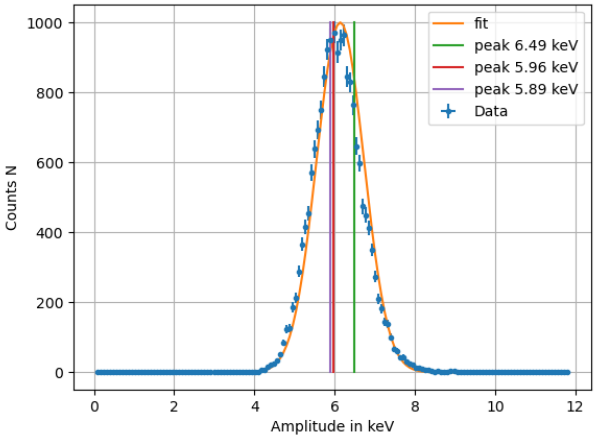

Figure 31: Amplitude distribution for channel 10 of batch 2 with marker lines for the calculated positions of the 5.89 keV, 5.96 keV and 6.49 keV peaks.

Channel	Batch-1 in keV	Batch-2 in keV	Batch-3 in keV
0	not	3.431±0.059	2.009±0.024
1	not	not	not
2	not	3.800±0.059	2.129±0.039
3	not	not	not
4	not	1.871±0.060	2.208±0.031
5	not	not	not
6	2.028±0.011	not	2.068±0.020
7	not	not	not
8	2.246±0.033	1.871±0.021	1.795±0.040
9	not	not	not
10	2.237±0.35	2.248±0.011	not
11	not	not	not
12	2.103±0.016	1.949±0.036	not
13	not	not	not
14	1.934±0.02	2.068±0.015	not
15	not	not	not

Table 6: Table showing the energy resolution in keV of each connected channel as calculated in the histograms of fig. 41.

Channel	Batch-1 in %	Batch-2 in %	Batch-3 in %
0	not	13.343±0.229	12.277±0.147
1	not	not	not
2	not	14.175±0.220	12.513±0.229
3	not	not	not
4	not	6.369±0.204	11.779±0.165
5	not	not	not
6	9.962±0.054	not	10.807±0.105
7	not	not	not
8	10.382±0.153	11.453±0.129	7.909±0.176
9	not	not	not
10	11.365±1.62	13.266±0.065	not
11	not	not	not
12	11.730±0.089	11.372±0.210	not
13	not	not	not
14	9.887±0.012	10.807±0.078	not
15	not	not	not

Table 7: Table showing the energy resolution in % of each connected channel as calculated in the histograms of fig. 41.

5. Conclusion

In this thesis, I investigated the parameters of a Low-Gain-Avalanche-Detector. This includes the noise, the rise time and the energy resolution.
Firstly, using the SAMPIC the LGAD was checked for noise in every channel, resulting in the finding of two minor forms of signals of which the origin could not be determined. As these signals rarely appear and are easily filtered out in the analysis software for actual signals of events, the signals are not further analysed. It is suspected that the signals originate in the power supply or other electronic components used in the experiment. Also found in later experiments but to be noted here are signals found in only four channels showing a singular form. These show in contrast to the earlier noise signals a higher repetition, and as they are only found in other ways also problematic channels are an indicator for the problems observed there. Those make the idea of an investigation into the origin of these signals an interesting possibility, but are not part of this thesis. In addition, at the end of the signal a fall off of the amplitude was observed which is allocated to the LGAD which influenced the noise level of the measured data. When the tail is cut, the average noise for each channel decreases because of the closer distribution around the baseline. Thus, for single values the noise for single values was calculated with the tail cut off, as a standard distribution of all values measured in a random trigger. The average noise thus could be calculated as $2.570\,\text{mV} \pm 0.371\,\text{mV}$ without the tail cut and as $1.802\,\text{mV} \pm 0.260\,\text{mV}$ with tail cut respectively, which is sufficient for measurements of low energy particles. More problematic could be depending on the particle the falling tail observed when determining the data itself. For measurements that require detection of the whole signal, this could, but does not necessarily, create problems in the future.
Secondly, measurements detecting particles were made, beginning with a long measurement trying to find cosmics. As the cross-section of the LGAD for these signals is so small that statistically representable measurements would only be possible for extended measurements over months, it was decided to move to an $^{55}_{26}\text{Fe}$ X-Ray. The measurements with the $^{55}_{26}\text{Fe}$ source allowed for good measurements and a greater source of comparable data.
For calculation of the rise time, the measured signal's rising edge was fitted using first a quadratic and then an exponential fit, both showing good results for the rise time. However, as the quadratic fit showed problems with the fitting and overall accuracy, the fitting method was changed. Now using the exponential fit as more datapoints behind the rising edge could be used, a more accurate fit was possible. The results show an average rise time of $0.964\,\text{ns} \pm 0.234\,\text{ns}$ which shows to be a very fast detection speed. The channels partially deviate from the mean value, suggesting that for precise measurements each channel should be tested individually.

The method of fitting the signal for calculation of the rise time can be further used well for calculation of the maxima of the signals. In addition, the $^{55}_{26}$Fe source allows an energy calibration to the average energy of about 5.9 keV. The average energy resolution, ignoring problematic channels, is at about 0.348 keV$\pm$0.084 keV or overall 11.082 %$\pm$2.862 %. As with the rise time, the channels deviate partially, suggesting that for precise measurements each channel should be tested individually. Nevertheless, the low resolution results in the problem that the second peak at 6.5 keV can not be distinguished of the main peak at 5.9 keV. As the energy resolution is not the main importance of the LGAD a very fine energy resolution was not expected and is acceptable.
Going forward, the problems and curious noise in channel 0,2 and 4 of batch 2, as well as channel 8 of batch 1 should be investigated. Nevertheless, the LGAD itself with the fast rise time and the good overall noise show great promise for future possible applications.

References

[18] 'Beam test measurements of Low Gain Avalanche Detector single pads and arrays for the ATLAS High Granularity Timing Detector'. In: *Journal of Instrumentation* 13.06 (June 2018), P06017–P06017. ISSN: 1748-0221. DOI: 10.1088/1748-0221/13/06/p06017. URL: http://dx.doi.org/10.1088/1748-0221/13/06/P06017.

[Col18] CBM Collaboration. *The Transition Radiation Detector of the CBM Experiment at FAIR : Technical Design Report for the CBM Transition Radiation Detector (TRD)*. Tech. rep. Facility for Antiproton and Ion Research in Europe GmbH Darmstadt, Oct. 2018. DOI: 10.15120/GSI-2018-01091.

[Ehr22] Felix Ehring. *Readout of fast signals with a multichannel sampling module*. Bachelor's Thesis. Sept. 2022.

[Gia23] Gabriele Giacomini. 'LGAD-Based Silicon Sensors for 4D Detectors'. In: *Sensors* 23.4 (2023). ISSN: 1424-8220. DOI: 10.3390/s23042132. URL: https://www.mdpi.com/1424-8220/23/4/2132.

[Her16] Norbert Wermes Hermann Kolanoski. 'Teilchendetektoren'. In: (Feb. 2016). DOI: 10.1007/978-3-662-45350-6. URL: https://link.springer.com/book/10.1007/978-3-662-45350-6.

[Krü+22] W. Krüger et al. 'LGAD technology for HADES, accelerator and medical applications'. In: *Nuclear Instruments and Methods in Physics Research Section A: Accelerators, Spectrometers, Detectors and Associated Equipment* 1039 (2022), p. 167046. ISSN: 0168-9002. DOI: https://doi.org/10.1016/j.nima.2022.167046. URL: https://www.sciencedirect.com/science/article/pii/S0168900222004697.

[Mof+18] N. Moffat et al. 'Low Gain Avalanche Detectors (LGAD) for particle physics and synchrotron applications'. In: *Journal of Instrumentation* 13.03 (Mar. 2018), p. C03014. DOI: 10.1088/1748-0221/13/03/C03014. URL: https://dx.doi.org/10.1088/1748-0221/13/03/C03014.

[Sch00] Ulrich Schötzig. 'Half-life and X-ray emission probabilities of 55Fe'. In: *Applied radiation and isotopes : including data, instrumentation and methods for use in agriculture, industry and medicine* 53 (Oct. 2000), pp. 469–72. DOI: 10.1016/S0969-8043(00)00166-4.

[Sch19] Peter Schleper. '7 Detektoren zur Messung elementarer Teilchen'. In: (ws2018/19). URL: https://www.physik.uni-hamburg.de/en/iexp/gruppe-schleper/lehre/physik5-ws1819/documents/physik5-ws1819-seite72-95.pdf.

[Sun+20] Quan Sun et al. *The Analog Front-end for the LGAD Based Precision Timing Application in CMS ETL*. 2020. arXiv: 2012.14526 [physics.ins-det].

Declaration of Academic Integrity

I, Robert Jesse Kossmann, hereby confirm that this thesis, entitled "Investigations of a timing silicon particle detector" is solely my own work and that I have used no sources or aids other than the ones stated. All passages in my thesis for which other sources, including electronic media, have been used, be it direct quotes or content references, have been acknowledged as such and the sources cited. I am aware that plagiarism is considered an act of deception, which can result in sanction in accordance with the examination regulations.

Münster, January. 23. 2023

Robert Jesse Kossmann

I consent to having my thesis cross-checked with other texts to identify possible similarities and to having it stored in a database for this purpose. I confirm that I have not submitted the following thesis in part or whole as an examination paper before.

A. Appendix

A.1. Electrical devices

Figure 32: Used device as high voltage source.

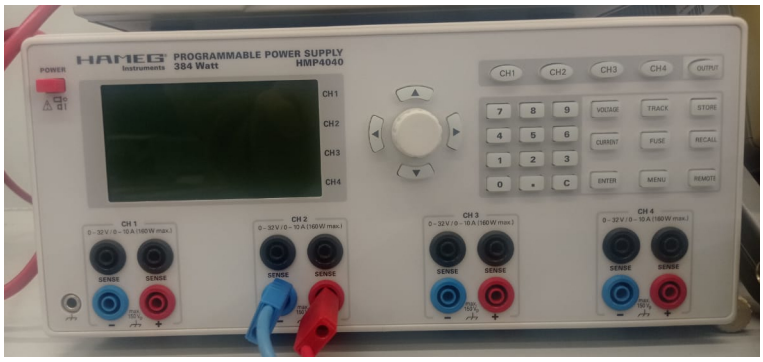

Figure 33: Used device as Low voltage source.

Figure 34: Used DAQ-device

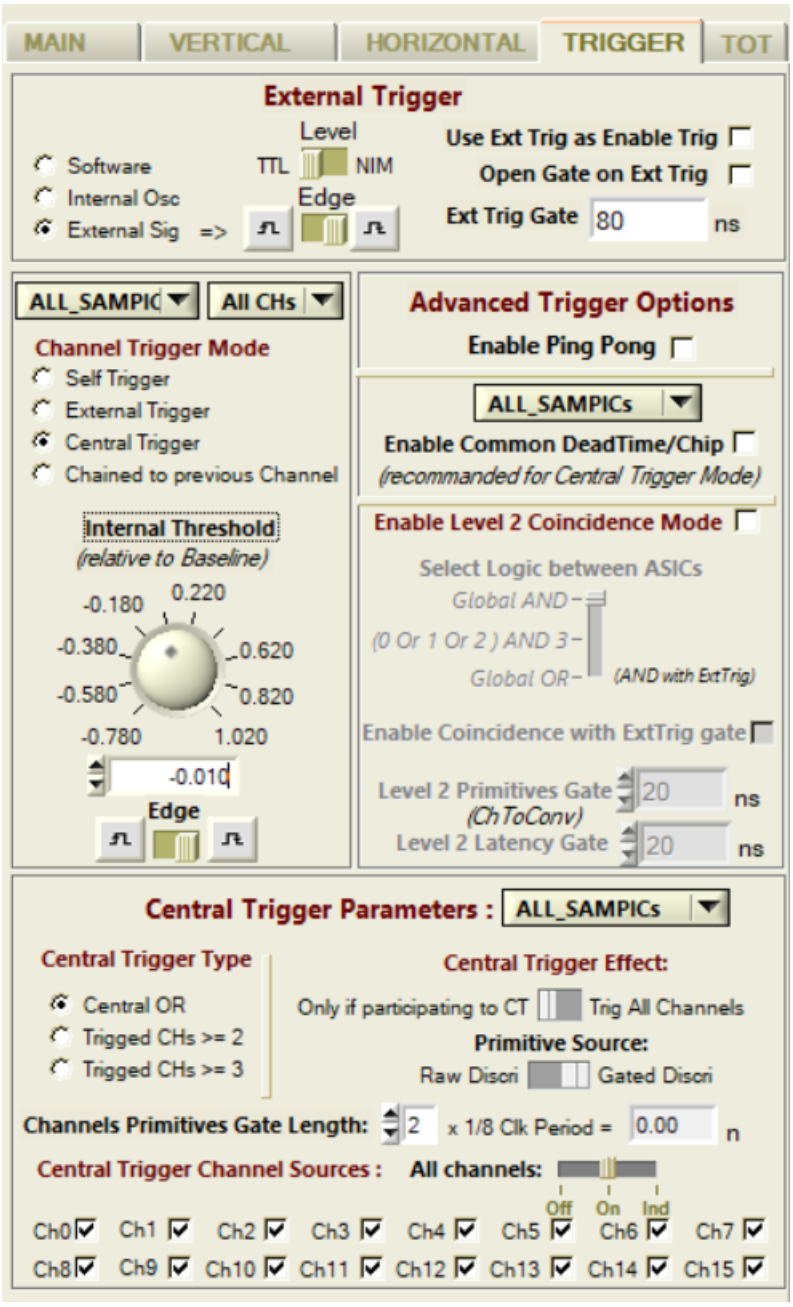

Figure 35: Settings of the Trigger-page, for the SAMPIC of Software version 3.4.1.

A.2. Examples

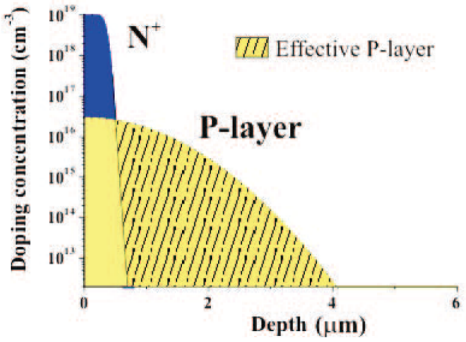

Figure 36: Doping concentration example for p- and n-dotation of the inner amplification area. The figure is taken from source [Mof+18].

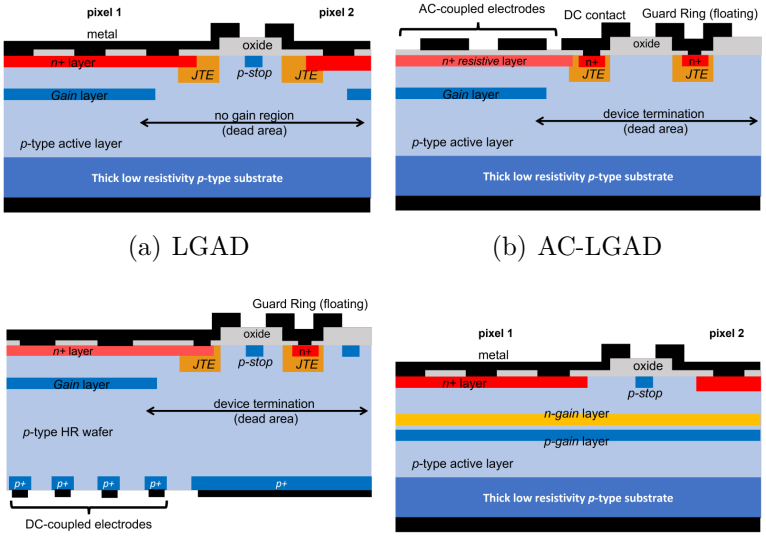

(a) LGAD (b) AC-LGAD

(c) i-LGAD (d) Dj-LGAD

Figure 37: Schematics for the LGAD variants as well as a standard LGAD for comparison, taken from source [Gia23].

A.3. Graphs

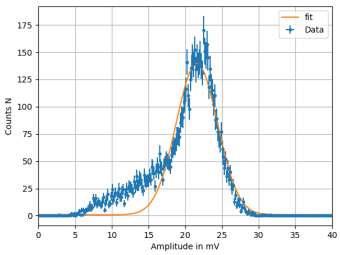

(a) Data: 0-8000

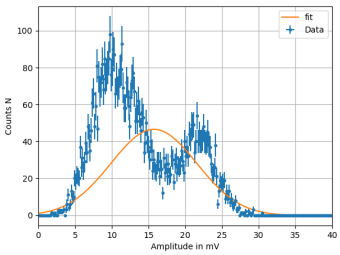

(b) Data: 8000-16000

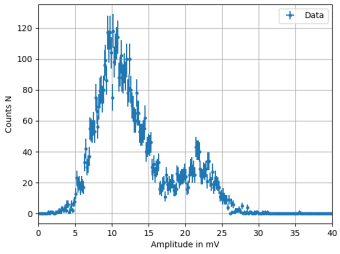

(c) Data: 16000-24000

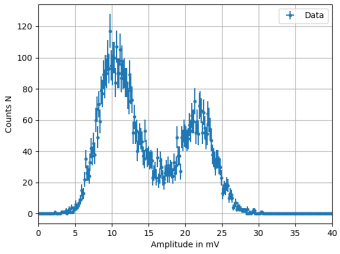

(d) Data: 24000-32000

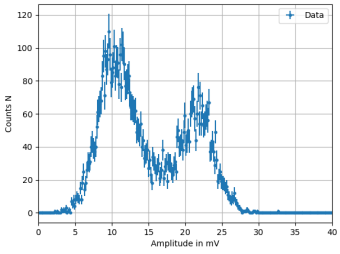

(e) Data: 32000-40000

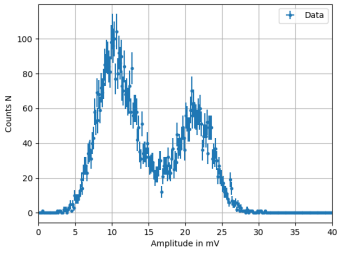

(f) Data: 40000-48000

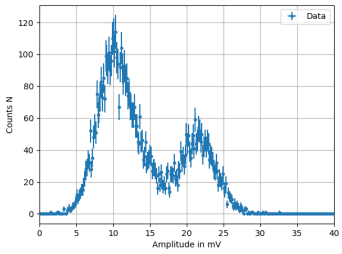

(g) Data: 48000-56000

Figure 38: The distributions over time from channel 8 of batch 1 in 8000 datapoint steps.

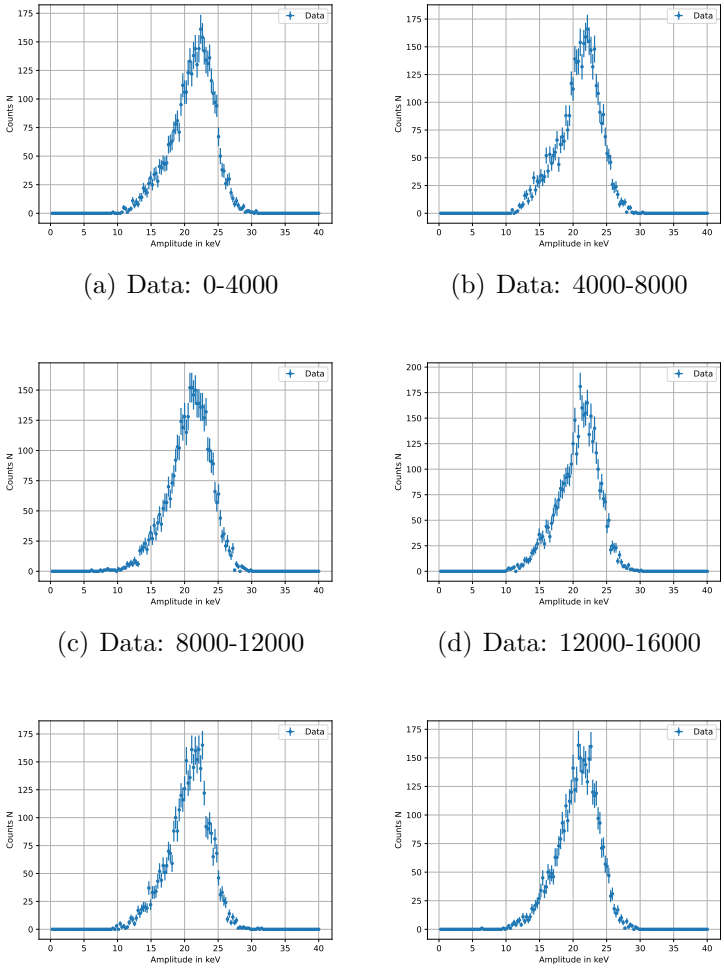

(a) Data: 0-4000

(b) Data: 4000-8000

(c) Data: 8000-12000

(d) Data: 12000-16000

(e) Data: 16000-20000

(f) Data: 20000-24000

Figure 39: The distributions over time from channel 10 of batch 1 in 4000 datapoint steps.

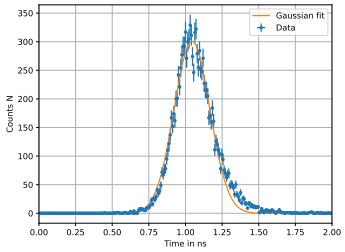

(a) Batch 1 channel 6

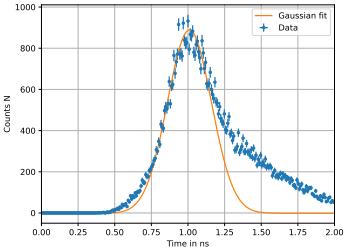

(b) Batch 1 channel 8

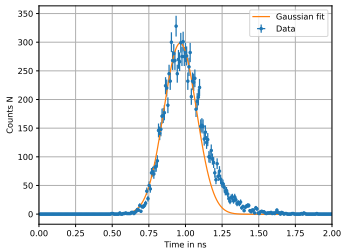

(c) Batch 1 channel 10

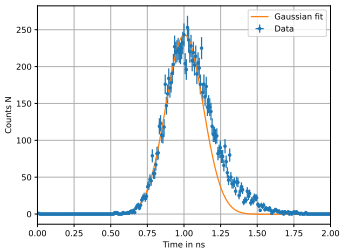

(d) Batch 1 channel 12

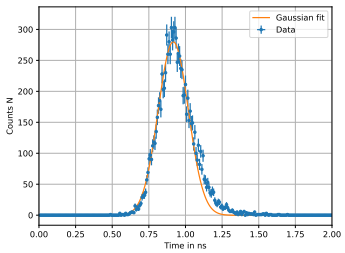

(e) Batch 1 channel 14

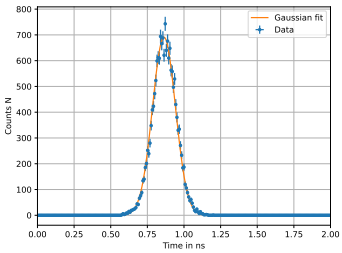

(f) Batch 2 channel 0

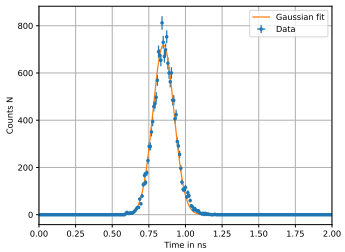

(a) Batch 2 channel 2

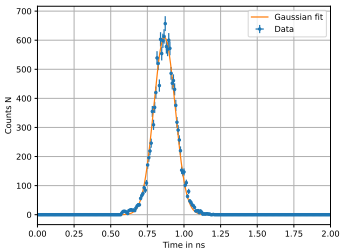

(b) Batch 2 channel 4

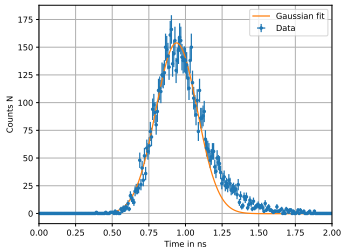

(c) Batch 2 channel 8

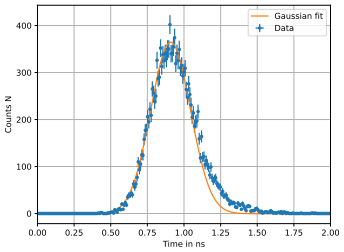

(d) Batch 2 channel 10

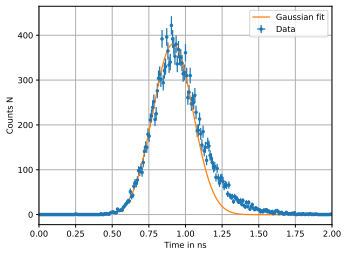

(e) Batch 2 channel 12

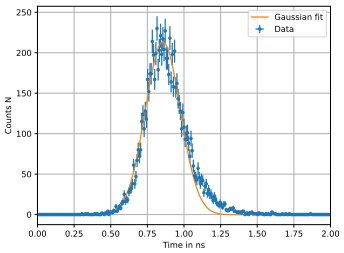

(f) Batch 2 channel 14

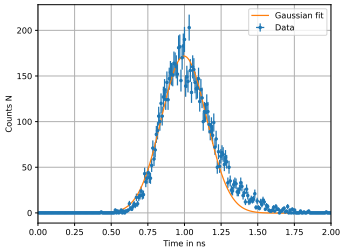

(a) Batch 3 channel 0

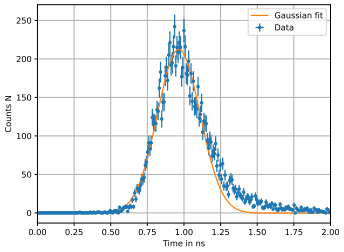

(b) Batch 3 channel 2

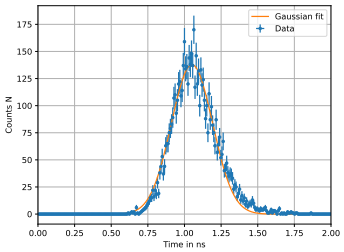

(c) Batch 3 channel 4

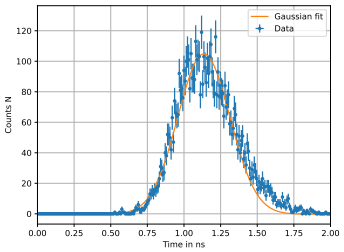

(d) Batch 3 channel 6

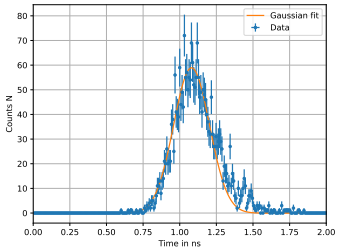

(e) Batch 3 channel 8

Figure 40: Rise time distribution results for each channel.

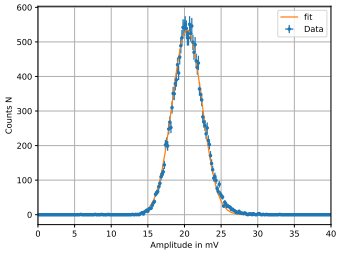

(a) Batch 1 channel 6

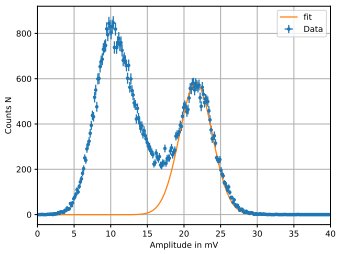

(b) Batch 1 channel 8

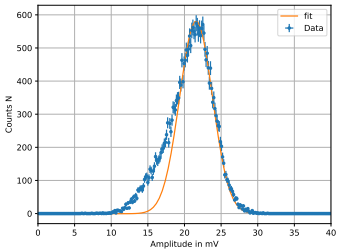

(c) Batch 1 channel 10

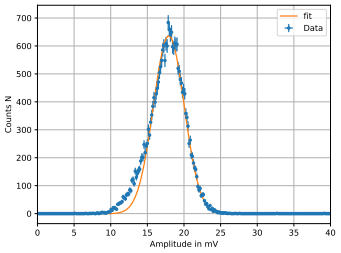

(d) Batch 1 channel 12

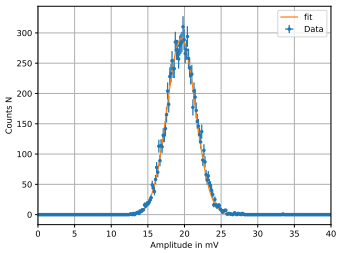

(e) Batch 1 channel 14

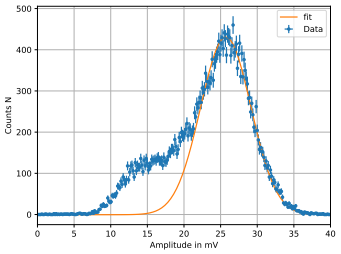

(f) Batch 2 channel 0

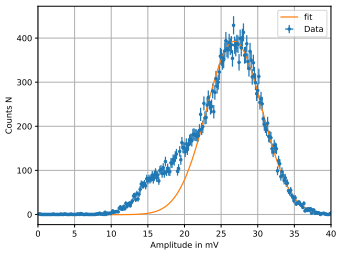

(a) Batch 2 channel 2

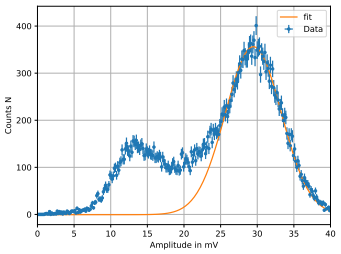

(b) Batch 2 channel 4

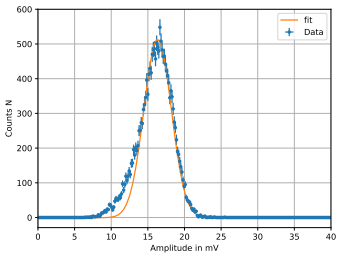

(c) Batch 2 channel 8

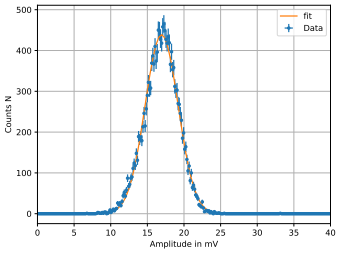

(d) Batch 2 channel 10

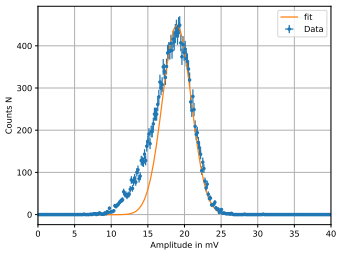

(e) Batch 2 channel 12

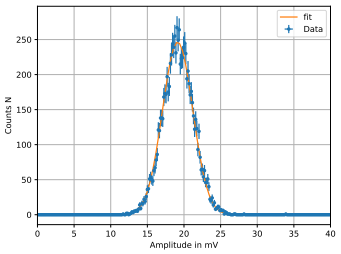

(f) Batch 2 channel 14

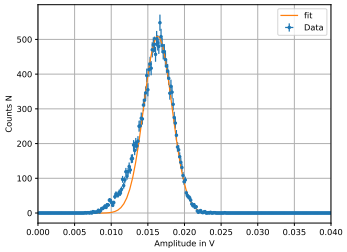

(a) Batch 3 channel 0

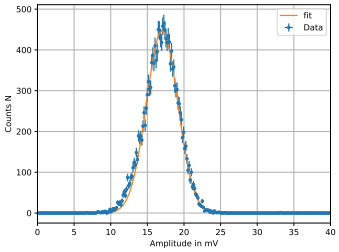

(b) Batch 3 channel 2

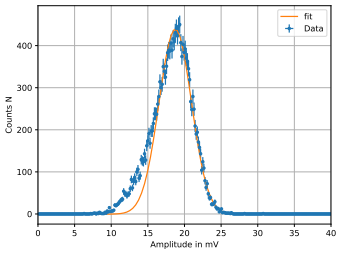

(c) Batch 3 channel 4

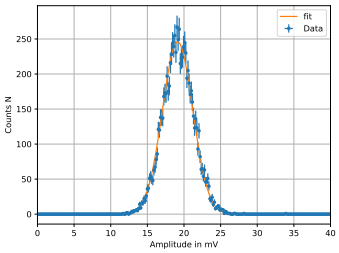

(d) Batch 3 channel 6

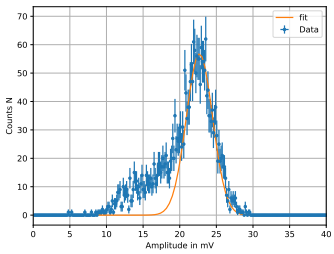

(e) Batch 3 channel 8

Figure 41: Amplitude distribution results for each channel.

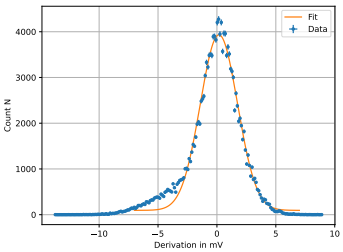

(a) Batch 1 channel 0

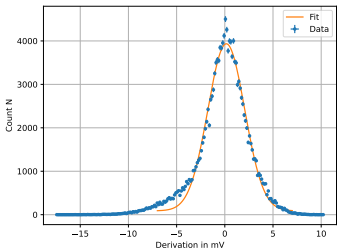

(b) Batch 1 channel 1

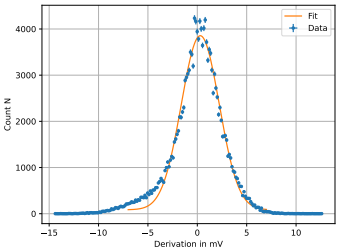

(c) Batch 1 channel 2

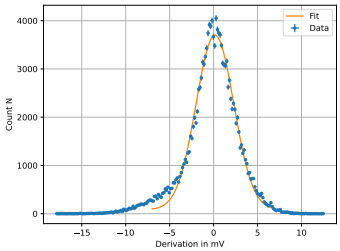

(d) Batch 1 channel 3

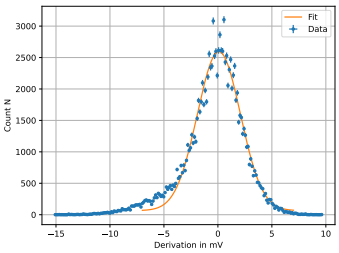

(e) Batch 1 channel 4

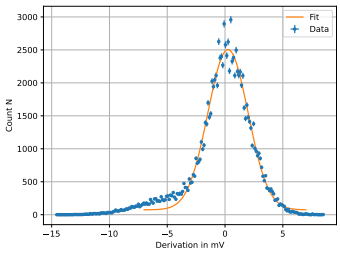

(f) Batch 1 channel 5

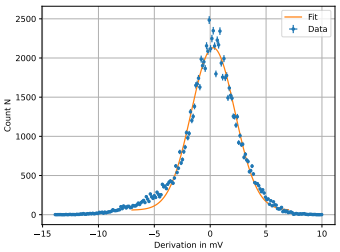

(a) Batch 1 channel 6

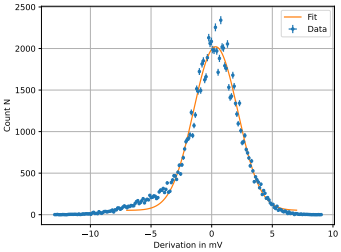

(b) Batch 1 channel 7

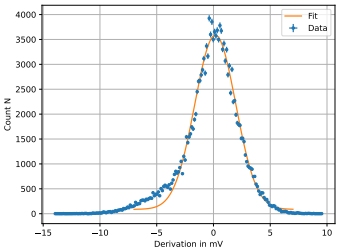

(c) Batch 1 channel 8

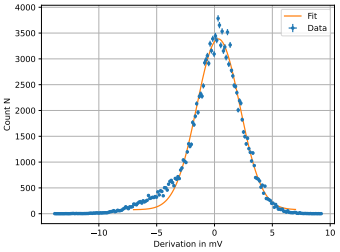

(d) Batch 1 channel 9

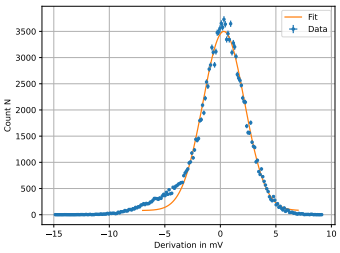

(e) Batch 1 channel 10

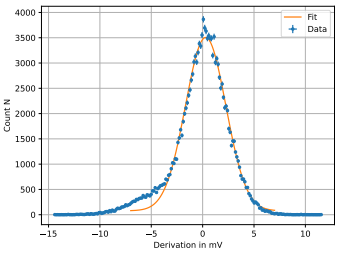

(f) Batch 1 channel 11

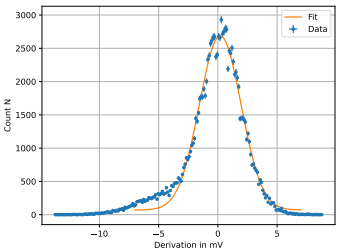

(a) Batch 1 channel 12

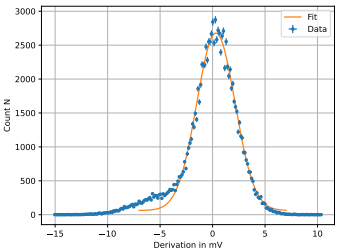

(b) Batch 1 channel 13

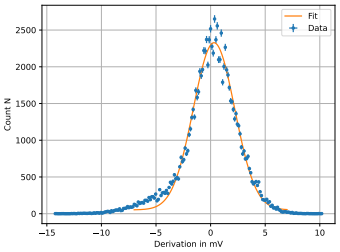

(c) Batch 1 channel 14

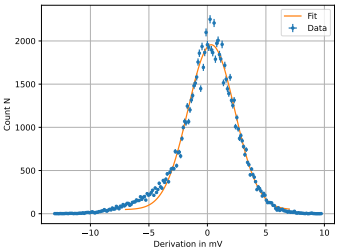

(d) Batch 1 channel 15

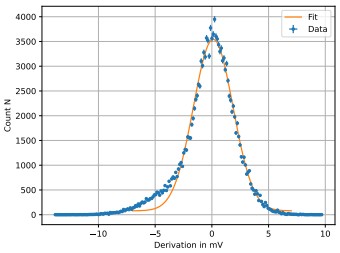

(e) Batch 2 channel 0

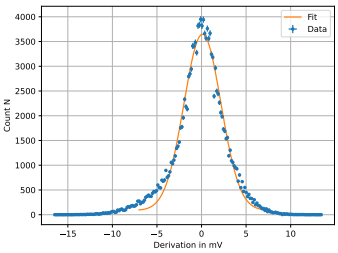

(f) Batch 2 channel 1

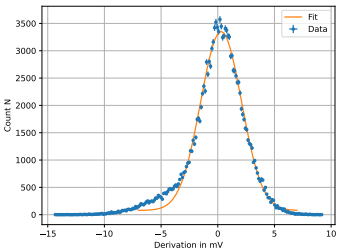

(a) Batch 2 channel 2

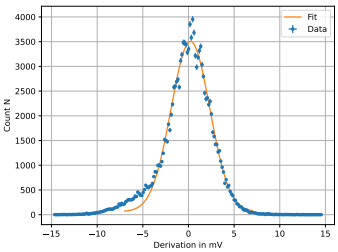

(b) Batch 2 channel 3

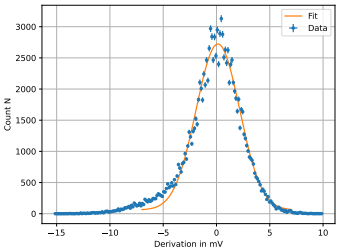

(c) Batch 2 channel 4

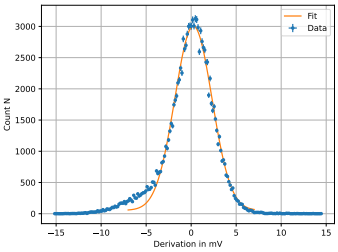

(d) Batch 2 channel 5

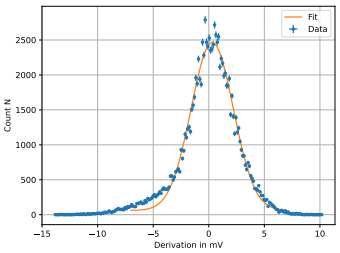

(e) Batch 2 channel 6

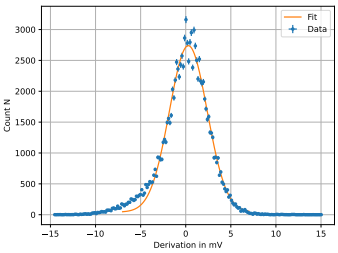

(f) Batch 2 channel 7

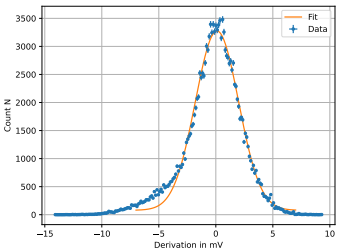

(a) Batch 2 channel 8

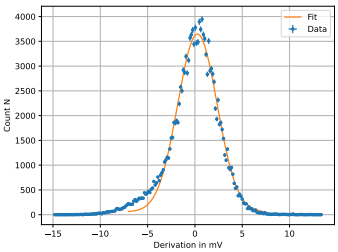

(b) Batch 2 channel 9

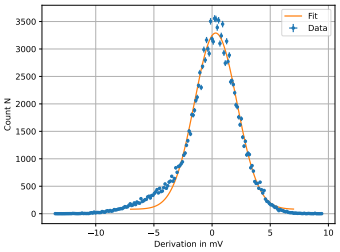

(c) Batch 2 channel 10

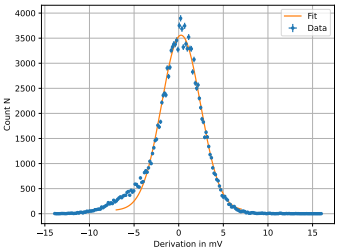

(d) Batch 2 channel 11

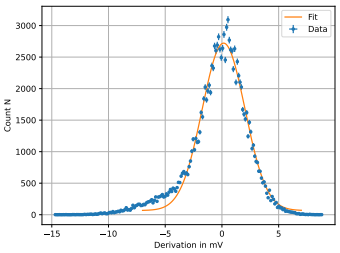

(e) Batch 2 channel 12

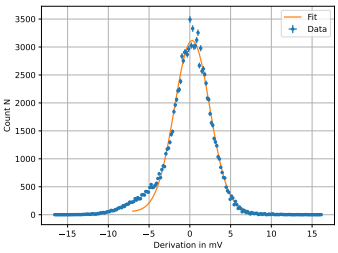

(f) Batch 2 channel 13

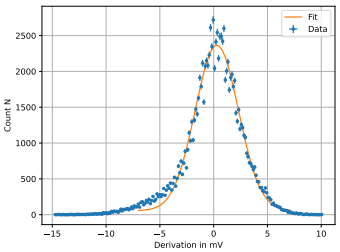

(a) Batch 2 channel 14

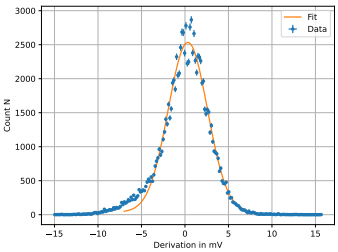

(b) Batch 2 channel 15

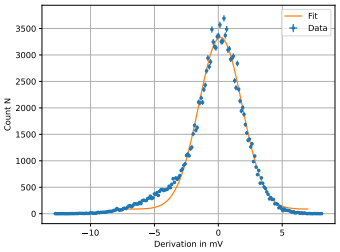

(c) Batch 3 channel 0

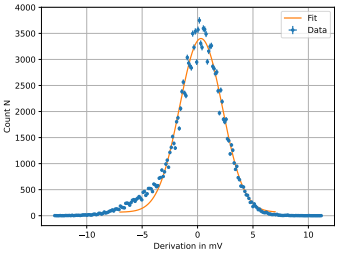

(d) Batch 3 channel 1

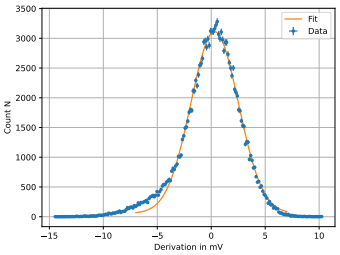

(e) Batch 3 channel 2

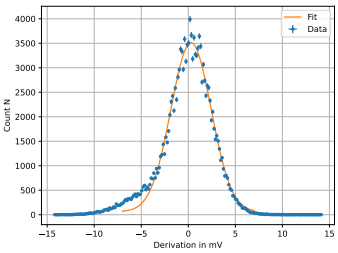

(f) Batch 3 channel 3

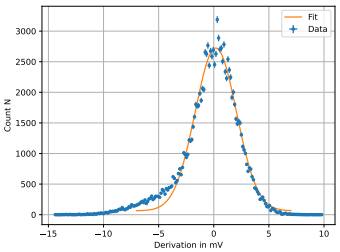

(a) Batch 3 channel 4

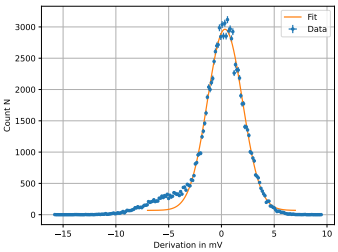

(b) Batch 3 channel 5

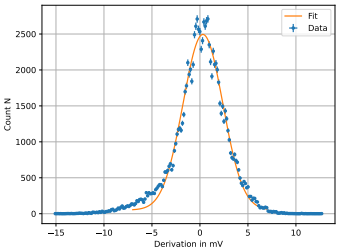

(c) Batch 3 channel 6

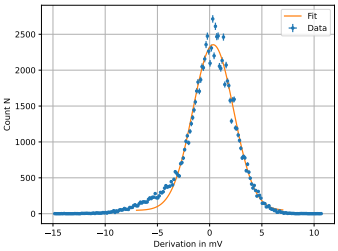

(d) Batch 3 channel 7

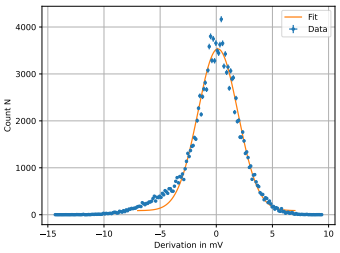

(e) Batch 3 channel 8

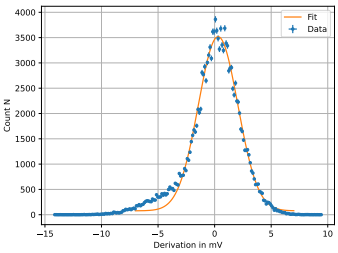

(f) Batch 3 channel 9

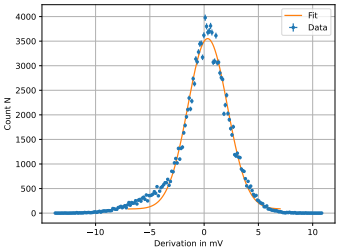

(a) Batch 3 channel 10

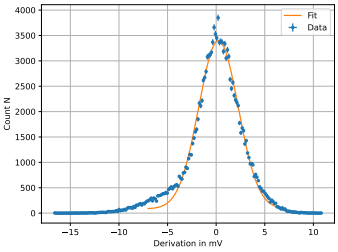

(b) Batch 3 channel 11

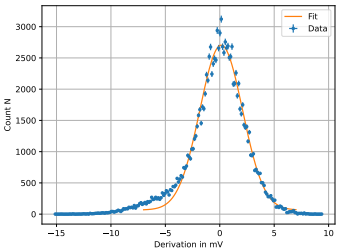

(c) Batch 3 channel 12

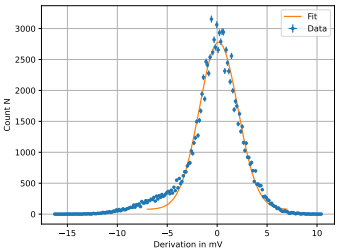

(d) Batch 3 channel 13

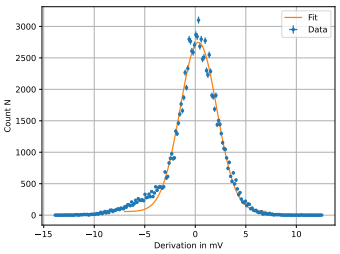

(e) Batch 3 channel 14

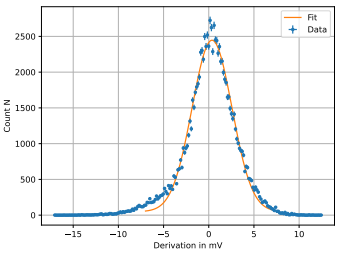

(f) Batch 3 channel 15

Figure 42: Uncut Noise histograms with fit for every channel.

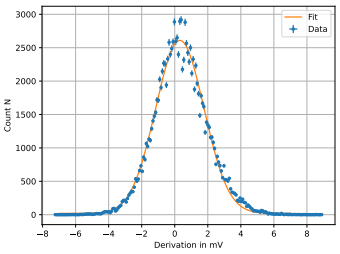

(a) Batch 1 channel 0

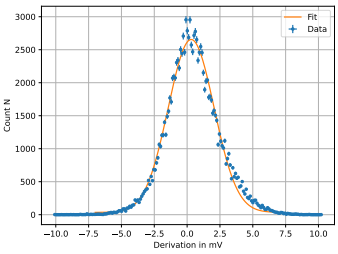

(b) Batch 1 channel 1

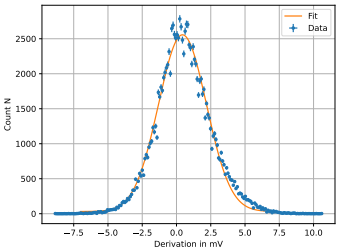

(c) Batch 1 channel 2

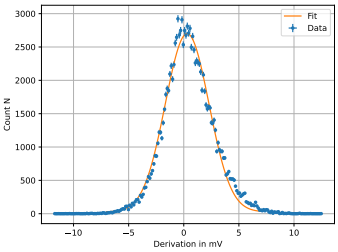

(d) Batch 1 channel 3

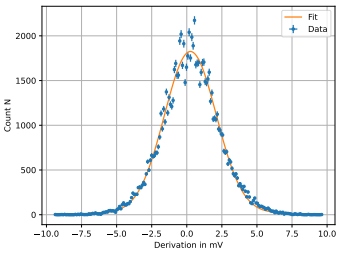

(e) Batch 1 channel 4

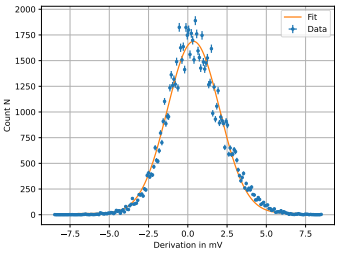

(f) Batch 1 channel 5

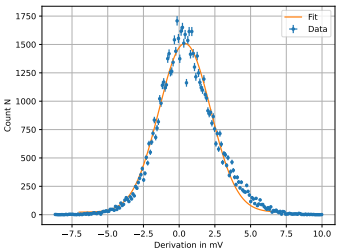

(a) Batch 1 channel 6

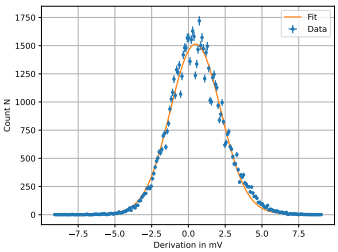

(b) Batch 1 channel 7

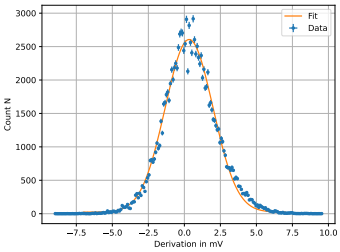

(c) Batch 1 channel 8

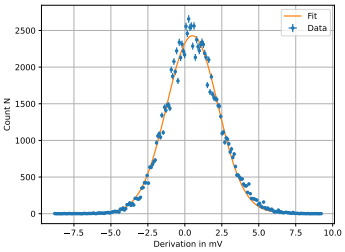

(d) Batch 1 channel 9

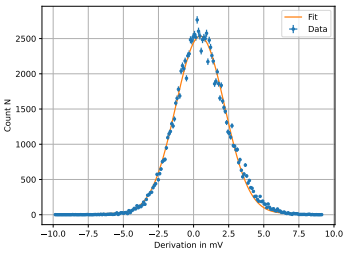

(e) Batch 1 channel 10

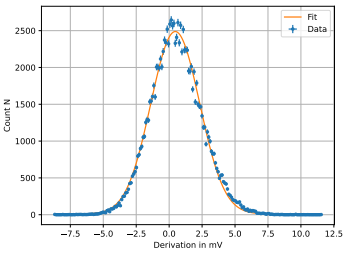

(f) Batch 1 channel 11

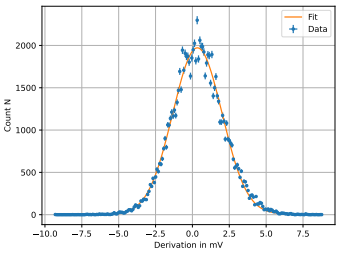

(a) Batch 1 channel 12

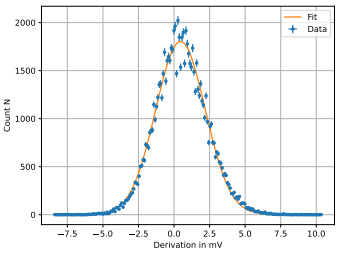

(b) Batch 1 channel 13

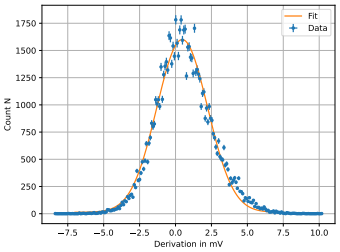

(c) Batch 1 channel 14

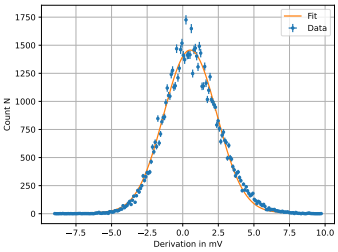

(d) Batch 1 channel 15

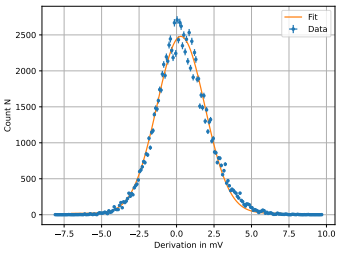

(e) Batch 2 channel 0

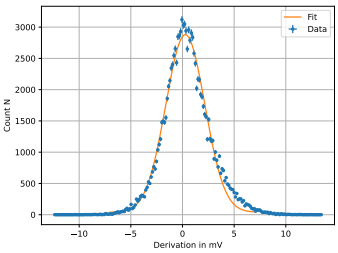

(f) Batch 2 channel 1

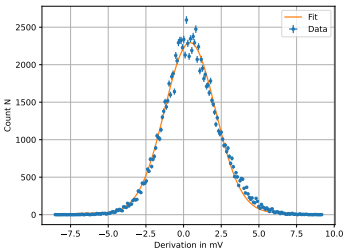

(a) Batch 2 channel 2

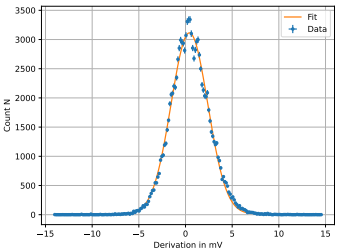

(b) Batch 2 channel 3

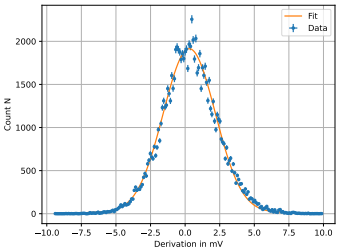

(c) Batch 2 channel 4

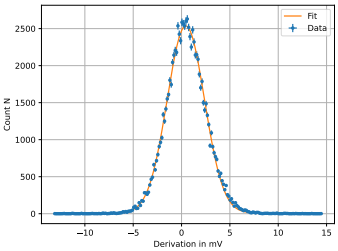

(d) Batch 2 channel 5

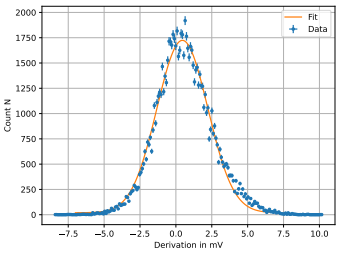

(e) Batch 2 channel 6

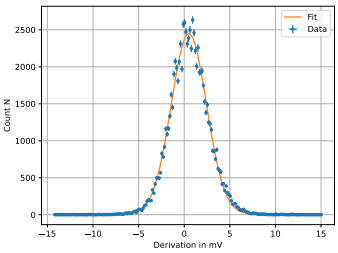

(f) Batch 2 channel 7

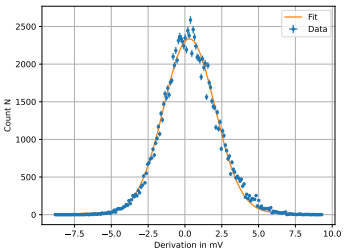

(a) Batch 2 channel 8

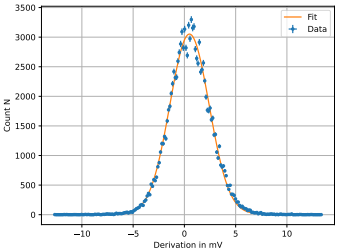

(b) Batch 2 channel 9

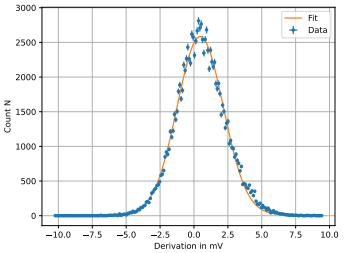

(c) Batch 2 channel 10

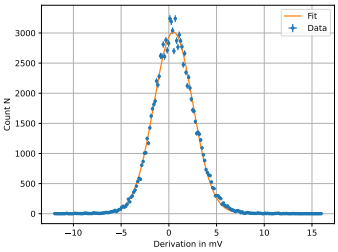

(d) Batch 2 channel 11

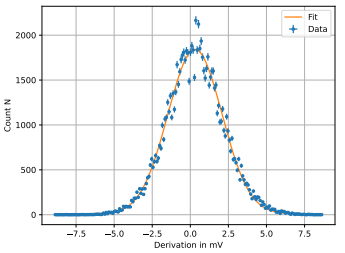

(e) Batch 2 channel 12

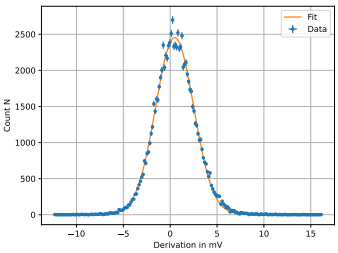

(f) Batch 2 channel 13

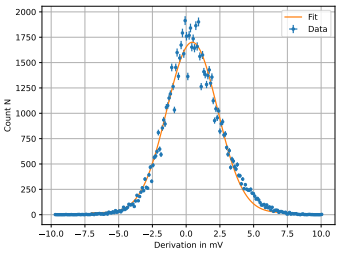

(a) Batch 2 channel 14

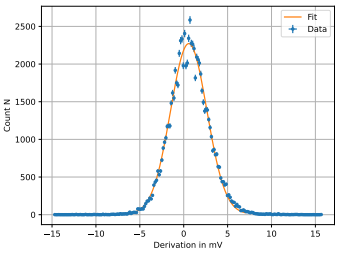

(b) Batch 2 channel 15

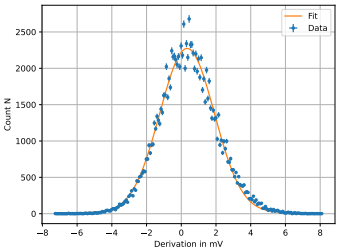

(c) Batch 3 channel 0

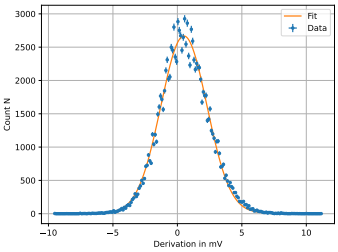

(d) Batch 3 channel 1

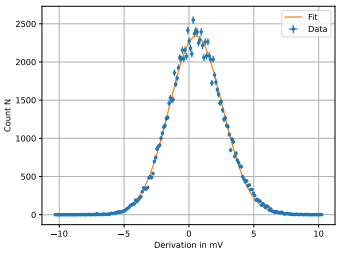

(e) Batch 3 channel 2

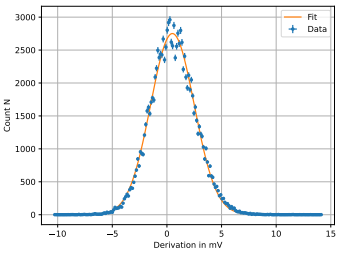

(f) Batch 3 channel 3

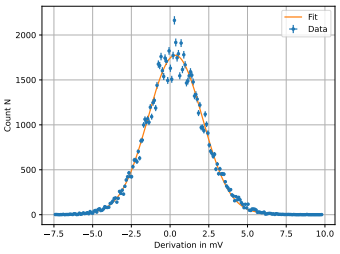

(a) Batch 3 channel 4

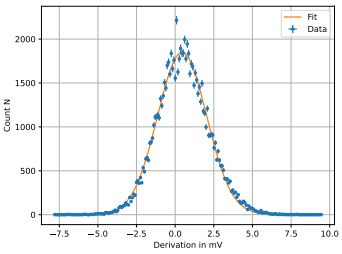

(b) Batch 3 channel 5

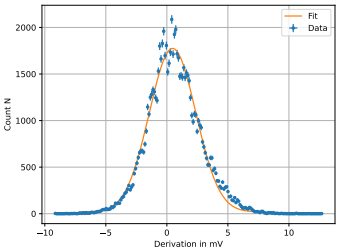

(c) Batch 3 channel 6

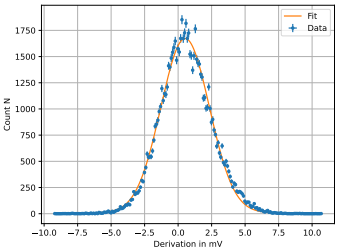

(d) Batch 3 channel 7

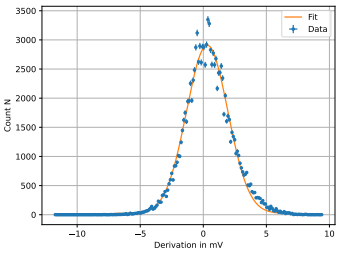

(e) Batch 3 channel 8

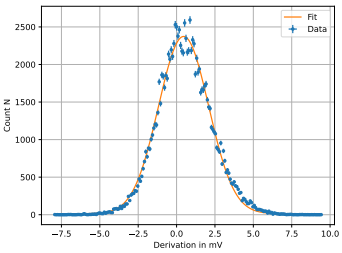

(f) Batch 3 channel 9

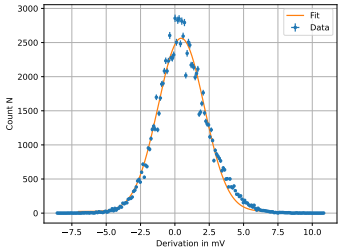

(a) Batch 3 channel 10

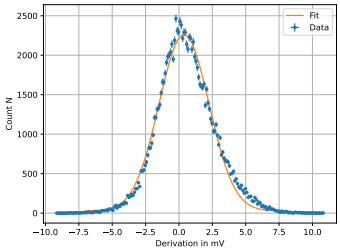

(b) Batch 3 channel 11

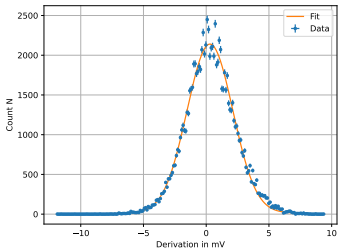

(c) Batch 3 channel 12

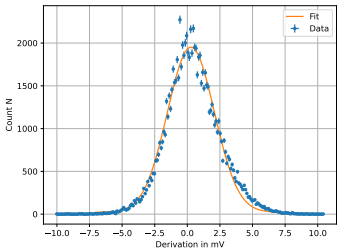

(d) Batch 3 channel 13

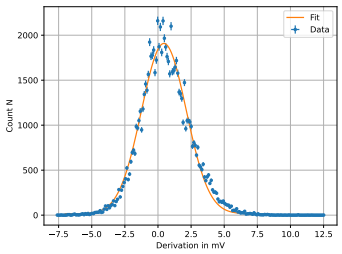

(e) Batch 3 channel 14

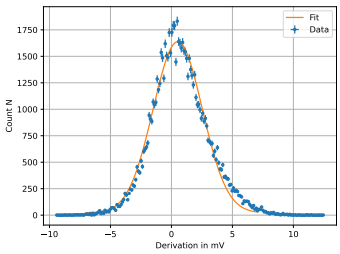

(f) Batch 3 channel 15

Figure 43: Noise histograms with fit for every channel and tail cutting.